GNXAS, a Multiple-Scattering Approach to EXAFS Analysis: Methodology and Applications to Iron Complexes

Tami E. Westre,[†] Andrea Di Cicco,[‡] Adriano Filipponi,[§] Calogero R. Natoli,[||] Britt Hedman,[†,⊥] Edward I. Solomon,[†] and Keith O. Hodgson[†,⊥]

Contribution from the Dipartimento di Matematica e Fisica, Università degli Studi di Camerino, Via Madonna delle Carceri, 62032 Camerino (MC), Italy, Dipartimento di Fisica, Università degli Studi dell' Aquila, Via Vetoio, 67010 Coppito, L'Aquila, Italy, INFN, Laboratori Nazionali di Frascati, C.P. 13, 00044 Frascati, Italy, and Department of Chemistry and Stanford Synchrotron Radiation Laboratory, Stanford University, Stanford, California 94305

Received January 10, 1994[⊗]

Abstract: GNXAS, a recently developed integrated approach to the analysis of EXAFS data is presented in detail. GNXAS provides for the direct fitting of theoretical signals (calculated by utilizing the Hedin-Lundqvist complex exchange and correlation potential and spherical wave propagators) to the experimental data. GNXAS is able to calculate all the signals related to two-, three-, and four-atom correlation functions with the proper treatment of correlated distances and Debye-Waller factors. The technique is particularly well-suited for the analysis of multiple-scattering effects and thus allows for accurate determination of bond distance and angular information of second and third neighbors. Herein we report the application of GNXAS to several chemical systems of known structure. The reliability of GNXAS was evaluated on a well-ordered inorganic complex, $Fe(acac)_3$, as well as a lower-symmetry coordination complex with mixed ligation, $Na[Fe(OH_2)EDTA]$. The total EXAFS signal generated by GNXAS matches closely the experimental data for both complexes, especially when all the multiple-scattering contributions were included in the theoretical signal. First neighbor distances obtained from refinement using GNXAS, as well as distances and angles for further neighbors, compared very well with crystallographic values. The angle dependence of the Fe-C-N multiple-scattering contribution in $K_3Fe(CN)_6$ was also examined. The results indicate that GNXAS can be used to determine angles relatively accurately for Fe-C-N configurations with angles greater than about 150°. These results establish the utility and reliability of the GNXAS approach and provide a reliable means to determine additional structural information from EXAFS analysis of structures of chemical interest.

Introduction

Extended X-ray absorption fine structure (EXAFS) spectroscopy is a valuable technique for investigating the local coordination environment of specific atomic species in systems ranging from metalloproteins[1,2] to catalysts.[3-5] The method is sensitive to short-range order (distances typically within about 3-5 Å of the absorber) and provides information on the distances to, numbers of, and types of neighboring atoms. EXAFS has the advantages of being able to focus on a selected type of atom and of being applicable to any physical state, including liquid or frozen solutions and amorphous solids. However, the analysis of EXAFS data requires accurately known experimental or theoretical pairwise phase and amplitude functions. Experimental standards have been widely used to extract reliable empirical amplitude and phase functions, and these have been used with success to obtain structural information from EXAFS data, particularly for nearest neighbors. Alternatively, reliable theoretical phases and amplitudes have recently become available that enable more information, including angular distributions, to be obtained from EXAFS analysis.

The empirical data-analysis technique[1,2,6,7] involves the use of pairwise phase and amplitude functions which have been extracted from the EXAFS data of suitable model complexes. The empirical technique allows for the determination of first neighbor distances with high accuracy (typically ±0.02 Å) but determines with less accuracy the coordination number (one atom in four or five) and the identity of the ligating atoms (not differentiating ±2 in Z). The empirical approach is of questionable utility for atoms beyond ~3 Å because of phase and amplitude transferability problems. A breakdown of the phase and amplitude transferability occurs because of intervening atoms that give rise to multiple-scattering (MS) signals. These MS signals can contribute significantly to the total EXAFS signal and very often interfere with the single-scattering (SS) signal. The MS effects are particularly evident when an intervening atom lies in a close-to-linear relationship with the absorber and a more distant scatterer, as occurs, for example, in Fe-oxo dimers[8] and metal carbonyls.[2,9-12] Multiple-scat-

[†] Department of Chemistry, Stanford University.
[‡] Università degli Studi di Camerino.
[§] Università degli Studi dell' Aquila.
[||] INFN.
[⊥] Stanford Synchrotron Radiation Laboratory.
[⊗] Abstract published in *Advance ACS Abstracts*, January 15, 1995.

(1) Cramer, S. P. In *X-ray Absorption: Principles, Applications, Techniques of EXAFS, SEXAFS and XANES*; Koningsberger, D. C., Prins, R., Eds.; John Wiley and Sons Inc.: New York, 1988; pp 573-662.
(2) Cramer, S. P.; Hodgson, K. O. *Prog. Inorg. Chem.* **1979**, *25*, 1.
(3) Lytle, F. W.; Via, G. H.; Sinfelt, J. H. In *Synchrotron Radiation Research*; Winick, H., Doniach, S., Eds.; Plenum Press: New York, 1980; Chapter 12.
(4) Lagarde, P.; Dexpert, H. *Adv. Phys.* **1984**, *33*, 567.
(5) Iwasawa, Y. *Tailored Metal Catalysts*; D. Reidel Publishing Co.: Dordrecht The Netherlands, 1986.
(6) Cramer, S. P.; Hodgson, K. O.; Stiefel, E. I.; Newton, W. E. *J. Am. Chem. Soc.* **1978**, *100*, 2748.
(7) (a) Scott, R. A. *Methods Enzymol.* **1985**, *117*, 414. (b) Shulman, R. G.; Eisenberger, P.; Kincaid, B. M. *Annu. Rev. Biophys. Bioeng.* **1978**, *7*, 559.
(8) Co, M. S.; Hendrickson, W. A.; Hodgson, K. O.; Doniach, S. *J. Am. Chem. Soc.* **1983**, *105*, 1144.
(9) Filipponi, A.; Di Cicco, A.; Zanoni, R.; Bellatreccia, M.; Sessa, V.; Dossi, C.; Psaro, R. *Chem. Phys. Lett.* **1991**, *184*, 485.
(10) Binsted, N.; Cook, S. L.; Evans, J.; Greaves, G. N.; Price, R. J. *J. Am. Chem. Soc.* **1987**, *109*, 3669.

0002-7863/95/1517-1566$09.00/0

tering effects can also be quite prominent for certain rigid ligands such as imidazoles and porphyrins[13,14] and can be of such magnitude that they dominate over SS signals even in structures that are not collinear (*vide infra*). Moreover, it can be difficult to obtain suitable models for extraction of reliable pairwise empirical amplitudes and phases because of the requirement for single well-ordered coordination shells that are separated from other EXAFS contributions. As a result of these limitations, determination of distances beyond the first coordination shell and of bond angles has been difficult using empirically-derived phase and amplitude functions.

An alternative to the empirically-based EXAFS data analysis is to calculate the phase and amplitude functions theoretically. In this approach, an expected theoretical signal is calculated assuming a structural model for the system under study. The resulting signal is then fit to the experimental data, varying the input parameters until a minimum of a selected reliability function is reached. The quality of the fit is further determined by inspection of EXAFS and Fourier transform (FT) residues. The theoretical approach is advantageous relative to the empirical approach in that MS contributions can be modeled and therefore bond distance and bond angle information from distant shells of atoms can in principle be determined. Also a theoretical approach is not dependent upon obtaining suitable model compounds to extract pairwise phase and amplitude functions. While the reliability of the results are limited by the accuracy of the theory, it is becoming clear that accuracy comparable to that available with the empirical technique is now possible as illustrated by this work and that published in some of the references cited below.

The GNXAS approach (where g_n stands for the n-atom distribution function and XAS stands for X-ray absorption spectroscopy) has been developed as an integrated theoretical approach to the analysis of EXAFS data.[15-17] Three distinctive features of the integrated GNXAS approach in comparison with other existing analysis packages (FEFF5[18,19] and EXCURVE[20]) are (1) an improved solution for the one-particle Green's function equation with complex optical potential of the Hedin–Lundqvist type in the muffin-tin approximation (from which the total photoabsorption cross section is calculated), (2) SS and MS signals are classified according to the appropriate n-atom distribution function with proper treatment of the configurational average of MS terms, and (3) the fit to the experimental spectrum is performed by comparing directly in energy space the raw data with a global model absorption coefficient that includes the structural signal, the edge jump normalization, the post-edge background, and if present, shake-up/shake-off edges, so that the structural signal is optimized together with other components of the absorption spectrum. These points will be illustrated individually in the course of the paper. Since GNXAS is able to calculate all the signals relating to two-, three-, and four-atom correlation functions with the proper treatment of correlated distances and Debye–Waller factors, it is particularly well-suited for the analysis of MS effects and for bond angle determination. GNXAS has been initially used on several simpler systems (including SiX_4, X = F, Cl, and CH_3,[21] $Os_3(CO)_{12}$,[9] Br_2 and HBr,[22] and brominated hydrocarbons[23]) and more recently on a complex polynuclear metal cluster[24] and several iron–nitrosyl complexes.[25]

In this paper, the background and brief theoretical description of the GNXAS methodology is presented, along with a description of the GNXAS programs and their use for analysis of molecular systems. The GNXAS methodology is followed by its specific application to three iron coordination complexes. These complexes were chosen to investigate the characteristics, advantages, and limitations of the method, in particular in the study of MS effects in chemical systems. Further, this detailed analysis enables an accurate error assessment by examining the variance between crystallographically known and EXAFS-determined metrical details.

The GNXAS method was applied to Fe K-edge EXAFS data for $Fe(acac)_3$, $Na[Fe(OH_2)EDTA]$, and $K_3Fe(CN)_6$ (where acac = acetylacetonate and EDTA = ethylenediaminetetraacetic acid). The applicability and utility of the GNXAS method was determined by studying the MS effects in the EXAFS data and evaluating the reliability of structural parameters (bond distances and angles) obtained from GNXAS. The study of the magnitude and complexity of MS contributions in the EXAFS data of $Fe(acac)_3$ was of particular interest since $Fe(acac)_3$, due to the regularity of its structure, has been widely used to extract both Fe–O and second-shell Fe–C phase and amplitude backscattering parameters for empirical EXAFS analysis. The empirical Fe–O backscattering parameters have been used quite successfully to model first shell iron–oxygen distances and coordination numbers in many iron-containing models and enzymes,[26-29] while the use of the Fe–C second-shell backscattering parameters has met with much more limited success[26,29] due to MS contributions. MS effects should be incorporated within the empirical functions approach in such a way that the phase and amplitude parameters reflect the exact geometry of the model compound and cannot be transferred to an unknown of different geometry. The GNXAS technique was also applied to $Na[Fe(OH_2)EDTA]$ to test the ability of GNXAS to interpret the EXAFS data for a lower-symmetry compound with mixed ligation, such complexes being a better approximation to the situation typically found in metalloenzymes, where the GNXAS approach can prove especially valuable in EXAFS data analysis. Finally, the EXAFS data of $K_3Fe(CN)_6$ was analyzed in detail with GNXAS to study the MS behavior of the linear Fe–C–N unit and to evaluate the use of this analytical approach for angle determination of small molecules liganded to transition metals. The results of these three applications together establish the validity and reliability of GNXAS as an approach for EXAFS

(11) Binsted, N.; Evans, J.; Greaves, G. N.; Price, R. J. *J. Chem. Soc., Chem. Commun.* **1987**, 1130.
(12) Teo, B. K. *J. Am. Chem. Soc.* **1981**, *103*, 3990.
(13) Co, M. S.; Scott, R. A.; Hodgson, K. O. *J. Am. Chem. Soc.* **1981**, *103*, 986.
(14) Hasnain, S. S.; Strange, R. W. In *Synchrotron Radiation and Biophysics*; Chichester, U.K., 1990; Chapter 4 and references therein.
(15) Filipponi, A.; Di Cicco, A.; Tyson, T. A.; Natoli, C. R. *Solid State Commun.* **1991**, *78*, 265.
(16) Filipponi, A.; Di Cicco, A. *Synchrotron Radiat. News* **1993**, *6*, 13.
(17) Filipponi, A.; Di Cicco, A. Unpublished data.
(18) (a) Rehr, J. J.; Albers, R. C.; Zabinsky, S. I. *Phys. Rev. Lett.* **1992**, *69*, 3397. (b) Rehr, J. J. *Jpn. J. Appl. Phys.* **1993**, *32*, 8.
(19) (a) Frenkel, A.; Stern, E. A.; Qian, A.; Newville, M. *Phys. Rev. B* **1993**, *48*, 12449. (b) Frenkel, A.; Stern, E. A.; Voronel, A.; Qian, A.; Newville, M. *Phys. Rev. Lett.* **1993**, *71*, 3485.
(20) Binsted, N.; Campbell, J. W.; Gurman, S. J.; Stephenson, P. C. SERC Darebury Laboratory EXCURVE92 program, 1991.
(21) Di Cicco, A.; Stizza, S.; Filipponi, A.; Boscherini, F.; Mobilio, S. *J. Phys. B* **1992**, *25*, 2309.
(22) D'Angelo, P.; Di Cicco, A.; Filipponi, A.; Pavel, N. V. *Phys. Rev. A* **1993**, *47*, 2055.
(23) Burattini, E.; D'Angelo, P.; Di Cicco, A.; Filipponi, A.; Pavel, N. V. *J. Phys. Chem.* **1993**, *97*, 5486.
(24) Nordlander, E.; Lee, S. C.; Wei, C.; Wu, Z. Y.; Natoli, C. R.; Di Cicco, A.; Filipponi, A.; Hedman, B.; Hodgson, K. O.; Holm, R. H. *J. Am. Chem. Soc.* **1993**, *115*, 5549.
(25) Westre, T. E.; Di Cicco, A.; Filipponi, A.; Natoli, C. R.; Hedman, B.; Solomon, E. I.; Hodgson, K. O. *J. Am. Chem. Soc.* **1994**, *116*, 6757.
(26) DeWitt, J. G.; Bentsen, J. G.; Rosenzweig, A. C.; Hedman, B.; Green, J.; Pilkington, S.; Papaefthymiou, G. C.; Dalton, H.; Hodgson, K. O.; Lippard, S. J. *J. Am. Chem. Soc.* **1991**, *113*, 9219.
(27) Hedman, B.; Co. M. S.; Armstrong, W. H.; Hodgson, K. O.; Lippard, S. J. *Inorg. Chem.* **1986**, *25*, 3708.
(28) Tsang, H. T.; Batie, C. J.; Ballou, D. P.; Penner-Hahn, J. E. *Biochemistry* **1989**, *28*, 7233.
(29) Scarrow, R. C.; Maroney, M. J.; Palmer, S. M.; Que, L., Jr.; Roe, A. L.; Salowe, S. P.; Stubbe, J. *J. Am. Chem. Soc.* **1987**, *109*, 7857.

data of chemical systems. Given this, the technique may be used to analyze unknown systems, as further elaborated in ref 25.

It should be noted here that other groups have developed analysis packages similar in concept to GNXAS. The program EXCURVE, developed at Daresbury, is probably the oldest.[20] The program FEFF,[30,31] developed at the University of Washington, Seattle, came later, roughly at the same time as GNXAS, initially with the possibility of calculating single scattering only, then including multiple scattering in later versions (FEFF5).[18,19] We shall briefly discuss the relationship of these programs to GNXAS in the course of the methodology presentation which follows.

GNXAS Methodology

Background. Until relatively recently, the lack of a proper theoretical formulation of the photoabsorption process has limited the use of theoretical functions for reliable analysis of EXAFS data. It was necessary to obtain a correct mathematical description of the spherical wave propagation of the photoelectron through the system (in an inner core photoabsorption process the photoelectron is created in an eigenstate of the angular momentum operator or a definite mixture of them) and to use an appropriate optical potential in describing this propagation. Early plane-wave SS theories[32] failed even in the high-energy limit[33] and had to be replaced with MS theories with spherical-wave propagation.[34-39] It was also realized that the "universal" atomic potentials used to calculate standard theoretical amplitudes and phases were not sufficiently reliable because the electrostatics was not modeled correctly. Therefore, it was necessary to construct a realistic charge density on and around the photoabsorber, as is done in band theory calculations. The Mattheiss[40] prescription of overlapping neutral atom charge densities provided charge densities that are acceptably close to those obtained by self-consistent procedures. The Coulomb, exchange, and correlation potentials could then be calculated from this cluster charge density.

Additionally, in the statistical interpretation, the local density approximation of the Hedin–Lundqvist[41,42] (HL) exchange–correlation potential proved to be a good starting point for the photoelectron optical potential. The HL exchange–correlation potential takes into account the energy dependence of the exchange and correlation (Coulomb) hole around the propagating electron in the dispersive (real) part and has an imaginary part capable of reproducing the observed electron mean-free path in metals and semiconductors.[43] The optical potential could be approximated by the self-energy of a uniform interacting electron gas with a density given by the local density of the system. In the spirit of this statistical approximation, Lee and Beni[44] extended the HL potential, which was initially devised to describe exchange and correlation corrections to the Coulomb potential due to the valence charge only, to the atomic core. When put in context with other components of MS theory correctly formulated in presence of a complex effective potential, this statistical potential proved to be a good starting point for the photoelectron optical potential.[30,45-47] The effect of the intrinsic inelastic channels has not been included in the theory. However, a reasonable estimate of the size of this effect on the amplitude of the EXAFS signal is less than 10% of the total signal, which is acceptable.

Another essential ingredient for a correct EXAFS analysis is the proper description of structural correlations in a system and the possibility of doing configurational averages. EXAFS has an almost unique advantage over other structural techniques in that it can probe atomic correlation functions of order greater than 2, *i.e.* position correlations of more than two atoms at a time. In fact, diffraction techniques only probe the pair correlation function, since the technique is based on the weak coupling between the probe (X-rays, neutrons) and the system under study. The double-scattering events of the probe which would allow access to higher-order correlations are generally negligible. This is not the case with EXAFS, in that the primary probe (the photon) couples weakly enough with matter so that the simple "golden rule" is sufficient to describe the photoabsorption cross section. However, the secondary probe, *i.e.* the emitted photoelectron, can couple strongly with the atoms of the system so that, in addition to SS, MS becomes quite detectable and exploitable in many cases. This feature is shared by other techniques that use electrons either as a secondary probe (as in photoelectron diffraction) or as a primary probe (as in low-energy electron diffraction). A good description of the dynamical strong coupling of the electron and matter is not easy to obtain, but once this is achieved, the next step is to have a general method for describing geometric structural correlations. Since the MS series is known to converge slowly, it can be resummed in such a way that the interrelation between the dynamic and the structural parts of the theory is transparent (while at the same time improving the convergence rate). In GNXAS this has been accomplished by summing together all the terms in the series referring to the same set of atoms in all their equivalent configurations with respect to the photoabsorber. This sum is done so as to treat all the MS signals relating to definite structural configurations together to give the various n-atom correlation functions.[15-17,45-49] This involves a topological structural analysis that is done on the chemical structure under study. Moreover, an efficient way to perform proper thermal or structural configurational averages, using probability distributions that are either chosen *a priori* or conveniently parameterized, has been devised in this integrated approach to EXAFS analysis.[50]

GNXAS Theoretical and Analytical Approach. Before discussing how the GNXAS package functions, it is useful to present a brief derivation of the photoabsorption cross section for a cluster of atoms in physical terms. It will serve to define concepts, to give an intuitive feeling of what is actually going on in the process, and provides the background for understanding the angle-dependent aspects of MS and how they can be used to obtain geometric information.

(30) Mustre de Leon, J.; Rehr, J. J.; Zabinsky, S. I.; Albers, R. C. *Phys. Rev. B* **1991**, *44*, 4146.
(31) Rehr, J. J.; Mustre de Leon, J.; Zabinsky, S. I.; Albers, R. C. *J. Am. Chem. Soc.* **1991**, *113*, 5135.
(32) Lee, P. A.; Citrin, P. H.; Eisenberger, P.; Kincaid, B. M. *Rev. Mod. Phys.* **1981**, *53*, 769.
(33) Rehr, J. J.; Albers, R. C.; Natoli, C. R.; Stern, E. A. *Phys. Rev. B* **1986**, *34*, 4350.
(34) Müller, J. E.; Schaich, W. L. *Phys. Rev. B* **1983**, *27*, 6489.
(35) Schaich, W. L. *Phys. Rev. B* **1984**, *29*, 6513.
(36) Lee, P. A.; Pendry, J. B. *Phys. Rev. B* **1975**, *11*, 2795.
(37) Natoli, C. R.; Benfatto, M. *J. Phys., Colloq.* **1986**, *47*, C8–11.
(38) Vvedensky, D. D.; Saldin, D. K.; Pendry, J. B. *Comput. Phys. Commun.* **1986**, *40*, 421.
(39) Durham, P. J.; Pendry, J. B.; Hodges, C. H. *Solid State Commun.* **1981**, *38*, 159.
(40) Mattheiss, L. F. *Phys. Rev.* **1964**, *134*, A970.
(41) Hedin, L.; Lundqvist, S. *Solid State Phys.* **1969**, *23*, 1.
(42) Lundqvist, B. I. *Phys. Kondens. Mater.* **1967**, *6*, 193.
(43) Penn, D. R. *Phys. Rev. B* **1987**, *35*, 482.
(44) Lee, P. A.; Beni, G. *Phys. Rev. B* **1977**, *15*, 28.
(45) Tyson, T. A.; Hodgson, K. O.; Natoli, C. R.; Benfatto, M. *Phys. Rev. B* **1992**, *46*, 5997.
(46) Natoli, C. R. In *X-ray Absorption Fine Structure*; Hasnain, S. S., Ed.; Ellis Horwood: Chichester, U.K., 1991; pp 6–14.
(47) Tyson, T. A.; Benfatto, M.; Natoli, C. R.; Hedman, B.; Hodgson, K. O. *Physica B* **1989**, *158*, 425.
(48) Filipponi, A.; Di Cicco, A.; Benfatto, M.; Natoli, C. R. *Europhys. Lett.* **1990**, *13*, 319.
(49) Filipponi, A. *J. Phys.: Condens. Matter* **1991**, *3*, 6489.
(50) Benfatto, M.; Natoli, C. R.; Filipponi, A. *Phys. Rev. B* **1989**, *40*, 9626.

In an inner core photoemission process, an electron is created in a continuum state of definite angular momentum ($l = l_i + 1$) with an amplitude given by the corresponding dipole matrix element M_l and the electron propagates through the system with kinetic energy $E = \omega - I_c > 0$ and finally exits into the vacuum. Here, l_i is the angular momentum of the initial core level and only the stronger dipole-allowed transition to a final $l = l_i + 1$ state is considered, but the extension to the general case is straightforward. In the equation $E = \omega - I_c$, ω is the photon energy and I_c is the core ionization potential for which the charge of the system relaxes completely around the created core hole. Concomitant with this fundamental process that has most of the weight ($>\sim 0.7$) other processes can take place. Either (i) the system does not relax completely around the core hole but remains with an excess energy, ΔE, with respect to the lowest relaxed state, so that the photoelectron kinetic energy is $E = \omega - I_c - \Delta E$ (intrinsic processes) or (ii) the photoelectron can release ΔE to the system in its journey to the outside vacuum (extrinsic processes). The distinction between these two processes (channels) is purely conventional since from a quantum-mechanical point of view the two processes cannot be distinguished.

In an absorption measurement, the emitted photoelectron is not detected, rather the total number of created holes (the total cross section) is measured. This is equivalent to integrating over all the photoemitted electrons. The integration process suppresses all the electron paths that do not come back to the photoabsorber so that the observed modulations of the absorption coefficient are due to the interference (constructive or destructive according to the photoelectron energy) between the outgoing and returning photoelectronic waves. Only electrons in the completely relaxed (elastic) channel with the maximum available kinetic energy $E = \omega - I_c$ contribute to the effect. Therefore, in studying the modulations in the absorption coefficient, the propagation of the coherent electrons can be described through the introduction of an effective optical potential. In this way a truly many-body problem can be reduced to an effective and tractable one-electron problem. The total many-body absorption cross section can be written as[45]

$$\sigma_{mb}(E) = S_{in}(E)\, \sigma_e(E) \tag{1}$$

where $\sigma_e(E)$ is the one-electron absorption cross section in the elastic channel, calculated with the optical potential, and $S_{in}(E)$ describes the inelastic channels. Examples of inelastic channels are the shake-up or shake-off double-electron excitations.[51] These may need to be taken into account since they can distort the EXAFS signal. Notice that in this approach $\sigma_e(E)$ includes the many-body amplitude reduction factor S_0^2.[30,45]

As mentioned earlier, the construction of the one-electron optical potential, although in principle feasible, is very difficult. The one-electron optical potential should take into account both the extrinsic and intrinsic effects and their interference. Moreover, the potential needs to be simple and versatile enough to describe the many varied situations encountered in practical applications. On the basis of statistical considerations, it has been found that the HL potential[41,42] is a good starting point for approximating the optical potential.[30,45-47] In this approximation, the optical potential is complex. Its imaginary part $\Gamma(E)$ gives rise to a finite lifetime that describes the attenuation of the photoelectron wave in the elastic coherent channel due to the possibility of inelastic excitations of the system. Therefore, the optical potential acts as a medium that diffracts the coherent electron wave with its real part and attenuates it via the imaginary part.

(51) Stern, E. A.; Bunker, B. A.; Heald, S. M. *Phys. Rev. B* **1980**, *21*, 5521.

The attenuation process has the consequence that the actual size of the system probed by a photoelectron with wave vector k and kinetic energy $E = k^2$ reduces to a sphere around the photoabsorber with a radius roughly equal to the mean-free path $\lambda(E)$ of the electron probe at that energy. The mean-free path is linked to the imaginary part of the optical potential $\Gamma(E)$ through the relation[52,53]

$$\lambda(E)\ (\text{Å}) = \frac{E}{\Gamma(E)} \frac{1}{k\ (\text{Å})^{-1}} \quad \text{or equivalently}$$

$$\lambda(E)\ (\text{au}) = \frac{k\ (\text{au})^{-1}}{\Gamma(E)\ (\text{Ry})} \tag{2}$$

when atomic units are used for lengths and Rydberg units for energies.

In a one-electron picture it is necessary to start from the description of the potential associated with a cluster of atoms. Since in the statistical approximation the HL potential depends on the local density of the system under study, as does the Coulomb potential, a rapid and efficient way of generating such a density has to be devised. As mentioned before, the Mattheiss[40] prescription of overlapping neutral atom charge densities present in the molecular cluster is able to generate charge densities that are acceptably close to those obtained by self-consistent procedures. At this point, a further approximation is made to the charge density to simplify the solution of the one-electron Schrödinger equation. After partitioning the cluster space into touching spheres around the atoms, an outer sphere encircling all the cluster and an interstitial region in between, one spherically averages the charge density inside the atomic spheres and calculates an averaged charge density in the interstitial region. The potential is set to a constant in this latter region. This approximation is likely to distort the calculated signal within $\sim$30 eV of the absorption edge, but its effects diminish quite rapidly with increasing energy.

Having constructed the potential, the derivation of the one-electron photoabsorption cross section $\sigma_e(E)$ in eq 1 follows from the application of MS theory. The main results relevant to the present discussion are summarized here. The reader is referred to the Appendix for a more detailed derivation. The equation for $\sigma_e(E)$ can be written as

$$\sigma_e(E) = \sigma_0^l(E)[1 + \chi^l(E)] \tag{3}$$

where $\sigma_0^l(E)$ is the final state l, dipole-allowed, atomic absorption cross section for the photoabsorbing atom and $\chi^l(E)$ represents the contribution due to the other atoms in the cluster. GNXAS uses an improved solution for the one-particle Green's function equation with complex potential in the muffin-tin approximation, from which the photoabsorption cross section is calculated. In this scheme the total cross section can be written as the sum of two contributions, the first one having the form of an "atomic" cross section relative to the muffin-tin sphere of the photoabsorber, the second one being the contribution coming from the neighboring scatterers. However the latter does not factorize into an "atomic" cross section times a dimensionless structure signal, as is the case with a real potential, therefore the structural signal which appears in eq 3 has to be defined as the ratio of the two contributions. This is different from that used in other codes. In most cases, this difference is negligible over almost the entire EXAFS spectrum but it may affect the amplitude of the structural signal in the low-energy part of the spectrum. For more details on this point the reader

(52) Müller, J. E.; Jepsen, O.; Wilkins, J. W. *Solid State Commun.* **1982**, *42*, 365.

(53) Müller, J. E.; Wilkins, J. W. *Phys. Rev. B* **1984**, *29*, 4331.

is referred to ref 45, eqs 3.8−3.12. In the region of convergence of the MS series the structural term $\chi^l(E)$ can be expressed as[45]

$$\chi^l(E) = \sum_{n=2}^{\infty} \chi_n^l(E) = \sum_{n=2}^{\infty} \sum_{p_n} \mathcal{A}_{p_n}^l(E; R_{ij}^{p_n}) \qquad (4)$$

where each $\chi_n^l(E)$ term represents the contribution originating from processes in which the excited photoelectron is scattered $n-1$ times by the surrounding atoms before returning to the photoaorber. Each $\chi_n^l(E)$ term is obtained by taking the imaginary part ($\mathcal{I}$) of the scattering amplitudes $A_{p_n}^l(E; R_{ij}^{p_n})$ relative to all the individual paths p_n of order n that involve at most n atoms, including the photoabsorber. Notice that the order is connected to the number of scattering events so that a path of order n may involve a number of atoms less than or equal to n, including the photoabsorber. In the curved-wave approximation,[33] valid for high energies and rather accurate at all energies for collinear and nearly collinear paths, the rules for writing the amplitude relative to a certain path are quite simple: (a) for each portion of the path, joining atoms i and j at distance R_{ij} insert a spherical wave propagator $\exp(i\kappa R_{ij})/(\kappa R_{ij})$ (where $\kappa = (E - \bar{V}_0)^{1/2}$ is the internal momentum and $\bar{V}_0$ the value of the (complex) interstitial potential); (b) for each site j, preceded by site i and followed by site k (therefore excluding the photoabsorber), insert an effective curved-wave scattering amplitude $f^j(\hat{R}_{ij} \cdot \hat{R}_{jk}; R_{ij}, R_{jk})$ depending on the angle between the two vectors $\hat{R}_{ij}$ and $\hat{R}_{jk}$ and their magnitudes R_{ij} and R_{jk}; (c) for the photoabsorber itself at site o, the amplitude $f_l{}^o$ should be the amplitude f^o defined as for the general atom in the path, projected on the final angular momentum l. With suitable generalization of the scattering amplitude f, these rules hold without approximation (see the Appendix for more details).

As a consequence, the functional form of the contribution of any path p_n is of the type

$$A_n^l(\kappa; R_{ij}^{p_n}) \sin[\kappa R_{p_n}^{\text{tot}} + \phi(\kappa; R_{ij}^{p_n})] \qquad (5)$$

where $R_{p_n}^{\text{tot}}$ is the total length of the path and $A_n^l(\kappa; R_{ij}^{p_n})$ and $\phi(\kappa; R_{ij}^{p_n})$ are, respectively, the amplitude and the phase of the signal associated with it. Due to the use of the optical complex potential $V(r)$, the amplitude of the path contains a damping factor which (in the Wentzel−Kramers−Brillouin (WKB) approximation for the potential phase shifts) can be written as

$$\exp[-\mathcal{I} \oint_{p_n} dr\, (k^2 - V(r))^{1/2}] \qquad (6)$$

where the integral is taken along the closed path of the photoelectron. Therefore, the longer the path, the more heavily its contribution is damped. Notice that the complex nature of the central atom phase shift has also been taken into account. In contrast, Lee and Beni[44] and Teo[12] only take into account the complex nature of the phase shifts for the backscattering atoms. These authors also only use the plane-wave approximation for the spherical-wave propagators. On the basis of eqs 3−5, the absorption cross section consists of the superposition of various oscillating signals of different amplitudes and periods onto a more or less smooth background given by the atomic absorption. The most important contributions coming from the various paths should be summed, and the resulting signal should be compared to the observed spectrum. However, the criterion of assessing the importance of the various contributions according to the number of scattering events, as suggested by the expansion in eq 4, is not of general validity since in some cases paths running along the same atoms with a different number of scattering events might contribute signals of similar strength.

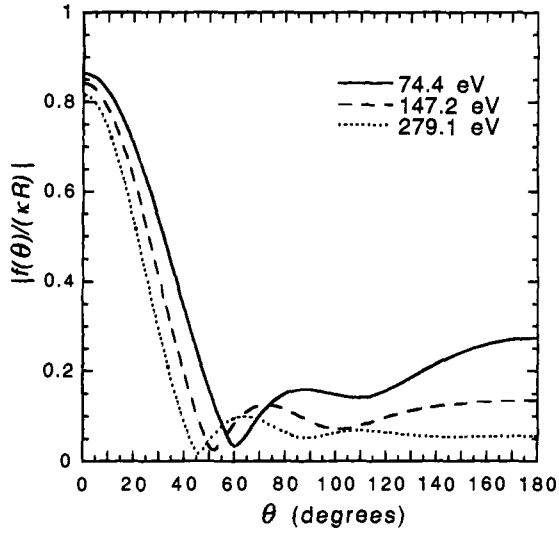

Figure 1. Plot of the expansion parameter $|f(\theta)/(\kappa R)|$ as a function of the scattering angle θ at different energies using the oxygen phase shifts and the Fe−O distance $R = 1.99$ Å for an Fe−O−C scattering pathway. The quantity $|f(\theta)/\kappa|^2$ is the effective scattering cross section for the excited photoelectron impinging onto the O atom at an angle θ away from the incoming Fe−O direction. From inspection of the behavior of this function, it is clear that forward scattering directions are enhanced by factors of 3−4. Notice that with this definition of the scattering angle θ the Fe−O−C angle is $180° - \theta$. This latter angle is indeed the one used throughout the paper for defining the bond angle in a triangle, besides the two short sides.

As presented in more detail in the Appendix, this might occur because the expansion parameter for the MS series, which is given by $|f(\theta)/(\kappa R)|$, where R is the typical nearest neighbor interatomic distance in the system, has a peculiar behavior as a function of the scattering angle θ. In fact, even at moderately high energies (≥200 eV), this quantity falls off quite rapidly from values on the order of unity in a forward cone of aperture ~20° to values typically on the order of less than 0.1. This behavior leads to the so-called "focusing effect", whereby forward scattering events enhance rather than depress the corresponding signal. In the case of a collinear path involving three sites o, i, and j at distance R from each other, the ratio of the triple-scattering signal to the double-scattering one is $2|f(0)/(\kappa R)|$. Therefore the amplitude of the fourth-order path is nearly twice that of the third-order, which in turn is twice that of second-order SS. At lower energies, the scattering becomes more isotropic and $|f(\theta)/(\kappa R)|$ may attain sizable values (~0.2−0.4) for $\sim 30° < \theta < 180°$, as illustrated in Figure 1, so that the rate of convergence of the MS series is slower.

From these considerations, it is evident that the rate of convergence of the MS series is controlled by an interplay between (a) the strength of the scattering, which depends on the energy, (b) the number of scattering events and the angles at which the scattering events occur, (c) the electron damping, which in turn depends on the energy, the length of the path, and the types of atoms along the path, and (d) the degeneracy of the various paths. As mentioned in the Background section above, an efficient way to cope with this situation and one that improves the rate of convergence of the MS series is to sum together up to infinite order (or to the necessary order to get convergence) all the terms which refer to the same set of atoms in all their equivalent configurations with respect to the photoabsorber, starting with pairs of atoms, then triplets, quadruplets, and so on.[15−17,48,49] The cut-off distance which limits the size of the model cluster, and therefore the number of structural configurations to be taken into account, can be deduced by inspecting the FT of the experimental absorption

spectrum under consideration. A topological structural analysis of the cluster will then provide all the relevant configurations whose path lengths are less than the chosen cut-off distance.

On the basis of these considerations, the structural term, in eq 3, related to a cluster of N atoms with the photoabsorber in site o can be rewritten as[15-17,48,49]

$$\chi^I(E) = \sum_{i=1}^{N-1} \gamma^{(2)}_{(o,i)} + \sum_{i=1}^{N-1}\sum_{j>1}^{N-1} \gamma^{(3)}_{(o,i,j)} + \sum_{i=1}^{N-1}\sum_{j>i}^{N-1}\sum_{k>j}^{N-1} \gamma^{(4)}_{(o,i,j,k)} + \ldots = \gamma^{(2)} + \gamma^{(3)} + \gamma^{(4)} + \ldots \quad (7)$$

where $\gamma^{(2)}_{(o,i)}$, $\gamma^{(3)}_{(o,i,j)}$, and $\gamma^{(4)}_{(o,i,j,k)}$ are the proper two-atom, three-atom, and four-atom signals associated with configurations of two (o,i), three (o,i,j), and four (o,i,j,k) atoms, respectively. The idea here is to sum all the MS signals that refer to the same subclusters of atoms.

In general, the $\gamma^{(n)}$ signals can be defined through the terms of the MS series. For example, in the case of a two-atom signal involving atoms o (photoabsorber) and i

$$\gamma^{(2)} = \chi_2^{oio} + \chi_4^{oioio} + \chi_6^{oioioio} + \chi_8^{oioioioio} + \ldots O(\chi_{10}) \quad (8a)$$

where the leading term is the SS process with obvious meaning of the superscripts. Similarly for a $\gamma^{(3)}$ signal involving sites o, i, and j one has

$$\gamma^{(3)} = 2\chi_3^{oijo} + 2\chi_4^{oiojo} + \chi_4^{oijio} + \chi_4^{ojijo} + \ldots O(\chi_5) \quad (8b)$$

where the coefficients count the time reversal degeneracy of the paths. Usually $\gamma^{(2)}$ and χ_2 differ very little since the higher-order MS contributions are very small, thus the $\gamma^{(2)}$ signal often is referred to as the SS contribution. However $\gamma^{(3)}$ and $2\chi_3$ can be quite different due to the sizable contributions from the higher-order terms.

For higher-order $\gamma^{(n)}$ signals, only the terms $\chi_m(E)$, with $m \geq n$, appear in the infinite summation. Higher-order terms are meaningful only when the MS series converges (see the Appendix). Nevertheless, the n-body $\gamma^{(n)}$ signals can be defined independently. In a system with only two atoms, the $\gamma^{(2)}$ signal coincides with the total structural term $\chi(E)$. For such a system, one can carry out the matrix inversion of eq A12 of the Appendix.

For a triplet of atoms (o,i,j), the proper three-atom signal is defined by subtracting the lower-order terms

$$\gamma^{(3)}_{(o,i,j)} = \chi^{(o,i,j)} - \gamma^{(2)}_{(o,i)} - \gamma^{(2)}_{(o,j)} \quad (9)$$

This procedure can be used to define the higher-order $\gamma^{(n)}$ signals. In general, the evaluation of the n-atom terms $\gamma^{(n)}$ is obtained by calculating the total signal for n atoms and subtracting all the lower-order $m < n$ terms. The exact calculation of the $\gamma^{(n)}$ signals is obtained by performing matrix inversions for defined sets of two, three, or four atoms. A very fast algorithm based on the continued fraction expansion has been developed to calculate the total n-atom signals,[49] since it is difficult to perform such inversions at high energies, due to the high number of angular momenta needed. It is assumed that the rearranged MS series in eq 7 always converges, especially after proper configurational averaging of the individual terms.

Since the MS series can now be written in terms of n-atom signals, an average over all the configurations, whether thermal or structural, in the system can be written as[16,17,48]

$$\langle\chi(E)\rangle = \varrho_0 \int_0^\infty 4\pi r^2\, dr\, g_2(r)\, \gamma^{(2)}(r;E) + \varrho_0^2 \int 8\pi^2 r_1^2 r_2^2 \sin\theta\, dr_1\, dr_2\, d\theta\, g_3(r_1,r_2,\theta)\, \gamma^{(3)}(r_1,r_2,\theta;E) + \varrho_0^3 \int 8\pi^2 r_1^2 r_2^2 r_3^2 \sin\theta\, dr_1\, dr_2\, dr_3\, d\theta\, d\omega\, g_4(r_1,r_2,\theta,r_3,\omega) \times \gamma^{(4)}(r_1,r_2,\theta,r_3,\omega;E) + \ldots \quad (10)$$

where the various g_n are the n-atom correlation functions which give the probability of the occurrence of a given configuration as seen from the absorbing site. The distances r_i and angles θ and ω are the structural variables, which parameterize the relative position of n atoms at a time, and ϱ_0 is the average density of the system. Since the various g_n are not known *a priori*, unless a definite model to describe thermal or structural disorder is known, a decomposition can be made of the distribution functions into sums of well-defined peaks associated with particular n-atom configurations. To each peak there corresponds a $\gamma^{(n)}$ signal which is dependent on peak shape, where the peak shape is defined by a certain number of parameters that can be varied during the fitting procedure. An initial background structural model must exist to establish such a decomposition. For molecules of biological interest, the various bond lengths and the angle between the bonds are the natural variables to describe thermal disorder and the various peaks can be described in terms of correlated Gaussian distributions. In this case, correlation variances and average distances and angles describing the various configurations can be fitted directly to the experimental signal.

Other ways of path selection and configuration averaging are obviously possible, and each code uses different criteria. FEFF5,[18,19] for example, retains only the most significant MS paths in order to avoid unnecessary computations. The default presorting criterion for retaining a path is that the amplitude of the contribution of a given path, estimated in the plane-wave approximation, is above 2.5% of the first-shell amplitude. Configurational averages are made via the method of cumulant expansion,[18,19] where the cumulants of various order enter among the fitting parameters. For instance, the first cumulant is the linear phase shift, the second is the Debye–Waller factor, the third is the cubic phase shift, etc. As is apparent from the previous discussion, we have instead chosen to classify MS paths according to a physical criterion that improves the convergence of the MS series and at the same time is suitable for configurational averaging. This approach has three advantages: (1) the number of structural parameters to be fit can be minimized (e.g., two bond lengths and an angle can serve to parameterize two SS scattering contributions and a MS contribution), (2) bond lengths and angles can be chosen as variables in the configuration space or given fixed values, and (3) correlations between the variables can be taken into account. In this respect, the cumulant expansion method is one of the possible choices in the GNXAS package for performing configurational averages.

GNXAS Programs. The GNXAS program set incorporates all the advances described above on *ab-initio* calculations of the X-ray absorption cross section and configurational averages and directly fits the theoretical results with the experimental EXAFS data. Raw data are compared directly in E space with a model absorption coefficient $\alpha_{mod}(E)$

$$\alpha_{mod}(E) = J\alpha_0(E)[1 + \chi(E)] + \beta(E) \quad (11a)$$

composed of an atomic absorption of hydrogenic type $\alpha_0(E)$, a structural $\chi(E)$ term, and an appropriate function $\beta(E)$. The function $\beta(E)$ accounts for remaining background effects and can include many-body features like double-electron excitation

channels (the $S_{in}(E)$ factor in eq 1). J is the absorption coefficient jump which takes into account thickness and density of the photoabsorbing centers of the particular sample. The comparison of the experiment with the theoretical cross section also requires the inclusion of a few parameters which do not have structural meaning. The XAS experiment is not a measure of the pure K-edge or L-edge absorption as there is always a background present mainly due to lower energy excitations and to instrumental effects. A smooth background is taken into account as a sum of polynomial functions. Also there are often spikes, steps, or small edges arising from instrumental effects or from intrinsic photoabsorption phenomena which are necessary to identify and to remove in the definition of the structural signal. It is possible to exclude particular energy regions affected by glitches, spikes, etc., and contributions coming from multielectron excitation channels can be included with arc tangent, steplike, or Lorentzian line shapes.

The procedure of fitting a global model absorption coefficient directly to the raw data is unique to the GNXAS package. In the usual approach, a structural signal $\chi(E)$ is separated from the measured absorption cross section $\alpha(E)$ according to the formula

$$\chi(E) = \{\alpha(E) - \alpha_0(E)\}/\alpha_0(E) \qquad (11b)$$

where $\alpha_0(E)$ is the absorption of an isolated embedded atom. This separation is achieved in three steps: (a) a pre-edge background removal that eliminates the energy dependence of the absorption other than the one under investigation; (b) a normalization to an edge jump that takes into account the thickness and density of the photoabsorbing atoms; (c) a post-edge background removal that eliminates the energy dependence due to the absorption from an isolated atom. This last step is the most crucial one as it can affect the final form of the structural signal. Up until recently, the practice followed was to perform the three steps without optimization in a partially subjective way. Recently a method has been suggested[54] that for the third step subtracts a spline that best eliminates the nonstructural, low-R portion of $\chi(R)$, the Fourier transform of $\chi(E)$, through an iterative procedure. Our approach has been instead to optimize all three steps in E space, since the three contributions cannot be separately defined in an unambiguous way, neither theoretically nor experimentally. The atomic cross section of the photoabsorber, for example, is a concept that can be defined theoretically in the framework of multiple-scattering theory only in the muffin-tin approximation for the cluster potential. However, the cross section so calculated contains unphysical oscillations due to the truncation of the atomic potential. In a non-muffin-tin approach of MS theory, there is no way to define unambiguously the central atom absorption, since this latter depends on the scattering amplitude of the region of space surrounding the photoabsorber, which is not well defined. The ideal situation would be to have a reliable theory that calculates altogether the pre-edge, edge, and post-edge absorptions, including the structural signal and shake-up/shake-off processes, to be fitted to the experiment. Unfortunately, this is too complicated and the present status of the theory is not yet sufficiently developed. However, we retain this concept by constructing a global model signal to fit to the whole absorption. It is true that the β term in eq 11a, which contains the pre-edge contribution plus shake-up/shake-off edges, couples this background to the structural model, but this is unavoidable and physical. In fact the method suggested in ref 54 has the drawback that it misrepresents the intensity and the shape of the double-excitation channels. Indeed, these spectral features peak in the low-R region of configuration space, since they contain high-frequency components. By trying to minimize this low-R nonstructural portion of $\chi(R)$ in order to define an optimal atomic background absorption, one is bound to misrepresent this contribution, since the intensity and the shape of the double-excitation channels are determined by the physics of the process.

The nonlinear fitting procedure is applied to the unfiltered data by a residual function

$$R_{N-n}(x_1,x_2,...x_n) = \frac{N}{N-n} \frac{\sum_{i=1}^{N}[\alpha(k_i) - \alpha_{mod}(k_i; x_1,x_2,...x_n)]^2 k_i^p}{\sum_{i=1}^{N}[\alpha(k_i)]^2 k_i^p} \qquad (12)$$

which is a χ-squared-like statistical function dependent on the structural and background parameters (x_1, x_2, ... x_n) and on the noise level. This function is not a true statistical χ^2 function since a true χ^2 function weights the data inversely according to the variance of each data point. However the two functions can be roughly proportional in a situation in which the collection times are such that all data points, at low and high k, have roughly the same variance, the latter being determined by calculating the standard deviation during averaging of the experimental spectra. This requires a careful selection of the experimental count times to ensure that high- and low-k data contribute significantly to the spectrum. In any case, in the GNXAS package, there is also the capability for generating error bars for each data point and constructing a true χ^2 function. In eq 12, $k = (E)^{1/2}$, N is the number of experimental points, and n is the number of fitting parameters. Structural parameters, such as equilibrium distances, angles, and Debye−Waller factors, can be refined around model values by using a Taylor expansion of phases and amplitudes up to sufficient order to calculate the theoretical signals relative to each new configuration in the refinement procedure. Signals need to be recalculated only when the structural parameters vary significantly (typically 10% or more) from the starting values. For details on applied nonlinear multiparametric fitting procedures, see ref 55.

It is useful to consider the number of independent data points present in a spectrum for comparison with the number of fit variables. At first sight, it would seem from eq 12 that this number is the total number of points; however, this is not so. In fact, doubling the number of points in a set of sinusoidal signals defined in k space does not lead to a doubling of the informational content in the spectrum, especially if one has already enough points to determine the phases and amplitudes. More quantitatively, if δk is the interval in k space where the spectrum is defined and if this latter is analyzed only on a finite interval δR of the conjugate variable R, then it has recently been shown[56] that the number of truly independent points N_I in a spectrum is given by $N_I = (2\delta k \delta R/\pi) + 2$. This conclusion does not contradict the procedure of nonlinear least-squares minimization in k space, since this latter is in principle able to lead to the determination not only of the number but also of the type of parameters relevant to the fit. In fact, trying to fit more parameters than the number allowed by the above formula will result in some of them being determined with very large errors, indicating which parameters are relevant. A parameter which is not relevant will not lead to a decrease of the squared residual function of the type shown in eq 12. Of course, it is very useful

(54) Newville, M.; Livins, P.; Yacoby, Y.; Rehr, J. J.; Stern, E. A. *Phys. Rev. B* **1993**, *47*, 14126.

(55) Bevington, P. R. *Data Reduction and Error Analysis for the Physical Sciences*; McGraw-Hill: New York, 1992.

(56) Stern, E. A. *Phys. Rev. B* **1993**, *48*, 9825.

to have an *a priori* estimate of the number of parameters one can reasonably fit to a spectrum as a guide, but in principle, this is not essential. In the data analysis section we shall indicate the independent data points to parameter ratio, which is an indication of the degree of determinacy of the fit, for each compound examined.

The inclusion of three-atom signals provides for determination of quantities such as bond angles, angle variances, and bond−bond and bond−angle correlations. The structural parameters associated with a pair of atoms are the distance R and the variance σ_R^2 (*i.e.*, the mean square variation of the distance R) if a Gaussian distribution of distances is used.[50] By considering the explicit contributions associated with triplets of atoms, one has to include three average quantities to define the triangle (*e.g.*, the two short sides R_1 and R_2 and θ, the angle between them). Thermal and configurational Gaussian disorder is taken into account through six parameters

$$\mathbf{M} = \begin{pmatrix} \sigma_{R_1}^2 & \sigma_{R_1R_2}^2 & \sigma_{R_1\theta}^2 \\ \sigma_{R_1R_2}^2 & \sigma_{R_2}^2 & \sigma_{R_2\theta}^2 \\ \sigma_{R_1\theta}^2 & \sigma_{R_2\theta}^2 & \sigma_{\theta}^2 \end{pmatrix} \tag{13}$$

which belong to the symmetric covariance matrix. In the case of a pair of atoms, the symmetric covariance matrix is represented by the variance σ_R^2. In a simple vibrational model for the two atoms, the DW factor in the EXAFS formula is given by $\exp(-2\sigma_R^2k^2)$. For a more complete treatment of configurational averages of a general EXAFS signal, the reader is referred to ref 50.

Besides the above structural parameters, other nonstructural parameters are to be refined in the fit (although their variation is limited by theoretical considerations). One of these nonstructural parameters is E_0, which aligns the experimental energy spectrum to the theoretical one. Physically E_0 is the origin of the photoelectron kinetic energy and should be defined as the core ionization threshold, I_c (vacuum level), so that $E = \omega - E_0$. Even though in the theoretical treatment an internal photoelectron wavenumber κ is defined relative to a muffin-tin origin $\bar{V}_0$, this origin is energy dependent (since the HL potential is energy dependent) and the only reason for its existence is that the true molecular potential has been approximated by its muffin-tin counterpart. Since non-self-consistent molecular charge densities are used, E_0 can be estimated only within an uncertainty of 2−3 eV. Self-consistent calculations might provide a more accurate determination of this quantity. However, the ionization threshold I_c is very seldom experimentally determined in current measurements of absorption spectra. Therefore, in practice, it is convenient to leave E_0 as a parameter in the fit. Another nonstructural parameter that can be varied in the fit is the many-body amplitude reduction factor S_0^2. The presence of S_0^2 is justified since intrinsic processes are not incorporated in the optical potential as described by the HL potential. The magnitude of S_0^2 should be related to the weight of the intrinsic processes in the absorption spectrum, which should be typically less than ~0.1. An additional source of broadening of the experimental spectra comes from the core hole width Γ_c that adds to the imaginary part of the potential. The value of Γ_c in the fit is usually kept fixed to some experimentally-determined value or good theoretical estimate.[57] Finally, the calculated signal should be convoluted with the experimental resolution function as determined by the specific optics of the experimental system used to measure the data.[58] In practice this function is modeled as a Gaussian with standard deviation E_r, which is allowed to vary in a range of 1−2 eV around the expected value.

Standard statistical concepts can be used to estimate the error affecting the fitted values of the parameters since the data analysis is performed using raw absorption spectra.[59,60] By neglecting systematic errors in the experimental data and in the theoretical calculations, the definition of the residual function given by eq 12 allows one to estimate parameter values, statistical standard deviations, and the quality of the fit. The expected value of this expression can be calculated in terms of the variance of the experimental and model signals. In particular, for $p = 0$, the expected value is the variance of the experimental points which is usually on the order of 10^{-6}−10^{-8}. This is the lower limit of the residual. Therefore, the quality of the fit is measured by the value of the residual. In the limit of a "perfect" simulation, the quality of the fit is on the order of the variance of the experimental data. Once the residual is near the variance of the experimental data, the statistical standard deviation of a specific structural parameter can be estimated by the increase of the residual as the parameter is varied. This kind of procedure is commonly used in multiparametric nonlinear fitting procedures. The statistical significance of the inclusion of particular fitting parameters can be tested by using the well-known F test, valid for χ^2 distributions.

These considerations do not take into account correlations between different fitting parameters. Correlation effects can increase the standard deviation of the measured parameters. A rigorous way to account for these effects is by estimating correlation through contour plots in parameter space.[61] However, the size of correlation effects can be greatly reduced by extending the number of independent points in the fitting procedure. Calculation of correlation among all the parameters is time consuming for standard data analysis. For EXAFS spectra recorded over a wide energy range and composed of a reasonable number of points, one can reasonably assume that correlations are within 3σ of the estimated standard deviation (σ). Error bars are estimated as three times the statistical standard deviation, an assumption that tends to overestimate the error. Usually the statistical errors determined are quite small. Systematic errors in the experimental data collection and the intrinsic limitation of the theory (arising mainly from the approximations) give rise to errors that can be much larger than the statistical ones. When GNXAS is applied to a particular class of unknown systems, the best indication would be the variance between GNXAS results on a number of similar structures for which crystallographic results are known. A thorough study of the effects of the approximations on the derived structural data is currently under way. According to our experience, from comparisons in fits to known, less complex structures, theoretical cross sections are quite accurate for the determination of distances and angles (on the order of 0.01 Å for bond distances, around 1° for bond angles) and are less accurate in the determination of covariance matrices (errors up to 10−20% for bond variances σ_R^2 have been observed). These limits are explored further in the applications described below for much more complex multishell transition metal complexes.

The GNXAS Program Set. The GNXAS package consists of five independent subprograms, each performing a specific

(57) Krause, M. O.; Oliver, J. H. *J. Phys. Chem. Ref. Data* **1979**, *8*, 329.

(58) The principal determining factor is the monochromator and associated vertical slit opening, with the resolution determined by the relationship $\Delta E/E = \cot(\Theta)\Delta\Theta$, where Θ is a function of the Darwin width and the vertical angular acceptance of the monochromator. The value of the Fe K-edge for the experimental conditions used for these experiments were ~1.0 eV.

(59) Di Cicco, A. Ph.D. Thesis, University of Rome "La Sapienza", 1991.

(60) Di Cicco, A.; Filipponi, A. Unpublished.

(61) Joyner, R. W.; Martin, K. J.; Meehan, P. *J. Phys. C* **1987**, *20*, 4005.

task in the general layout of the method described above. Briefly, in the order of application, the CRYMOL subprogram (a) generates a cluster of sufficient size to count all the two-, three-, and four-atom configurations associated with any nonequivalent photoabsorber up to a given cutoff with the correct degeneracy, so that one can define all the SS and MS paths involving up to four atoms and (b) selects the various types of atoms differing in atomic number, types of neighbors, and distances within a given tolerance to build appropriate miniclusters to be used in the construction of the overlapped charge density to obtain the potential.

The PHAGEN subprogram takes the minicluster generated by CRYMOL, defines muffin-tin radii according to Norman's criterion,[62] and uses the Mattheiss prescription to overlap self-consistent atomic charge densities to construct the cluster charge density. In order to model the charge relaxation around the core hole and to mimic the screening of the excited photoelectron, the self-consistent charge density of the photoabsorbing atom with one core hole and one electron added to the first nonoccupied valence state is used. On the basis of the cluster charge density obtained, the Coulomb and the HL exchange and correlation potentials are generated, the latter being recalculated at each new energy point. Finally, the radial Schrödinger equation is solved with the complex potential and the t atomic matrix elements calculated on the basis of eq A13 in the Appendix for any nonequivalent atom in the cluster.

The GNPEAK subprogram accepts as input a file generated by CRYMOL specifying the type, position, and neighbors of all the atoms in the cluster and searches for all two-, three-, and four-atom local configurations around each nonequivalent photoabsorber which are associated with SS and MS contributions to the absorption coefficient. These atomic configurations are referred to as peaks of the two-atom (g_2), three-atom (g_3), and four-atom (g_4) distribution functions. This information is passed to the GNXAS subprogram. The GNXAS subprogram also reads the atomic t matrix file generated by PHAGEN and calculates all the $\gamma^{(n)}$ signals relative to all the configurations calculated by GNPEAK.

Finally, the subprogram FITHEO builds up a model absorption signal (see eq 11) composed of an appropriate background plus the oscillatory structural contribution $\chi(E)$ already calculated by GNXAS. The parameters contained in the model absorption signal are then refined during a fitting procedure that tries to minimize the difference between the calculated and experimental signals. The function minimized is given by eq 12. Fits are done directly in E space. A standard statistical procedure commonly used in multiparametric nonlinear fitting is implemented here to perform χ^2 and F tests in order to answer typical questions arising in model refinements.

A comment is relevant on the relationship of GNXAS to other theoretical-parameter-based EXAFS analysis programs. EXCURVE, FEFF5, and GNXAS all have conceptual similarities regarding the calculation of SS and MS signals. All three programs at present use a theoretical scheme consisting of the reduction of the photoabsorption many-body problem to a one-particle problem with a complex Hedin–Lundqvist effective potential based on a charge distribution obtained by overlapping atomic charge densities following the Mattheiss prescription[40] in a muffin-tin approximation. The calculated signals are therefore in general very similar, with the differences arising from the definition of the muffin-tin parameters and the different way of defining the central atom absorption cross section mentioned above. A mere detailed comparison between the three packages beyond that pointed out in the sections above is outside the scope of this paper.

(62) Norman, J. G. *Mol. Phys.* **1976**, *31*, 1191.

Applications to Iron Complexes

Sample Preparation and Data Collection. $Fe(acac)_3$ was purchased from Aldrich, $K_3Fe(CN)_6$ was purchased from J. T. Baker, and $Na[Fe(OH_2)EDTA]$ was prepared according to the published procedures.[63] The crystalline samples were ground into a fine powder and diluted with BN. The BN powder mixture was pressed into a 1 mm thick slotted Al spacer and sealed with Mylar tape windows. The X-ray absorption spectra were recorded at the Stanford Synchrotron Radiation Laboratory on unfocused beamlines 7–3 and 4–3 during dedicated conditions (3 GeV, 25–90 mA). The radiation was monochromatized using a Si(220) double-crystal monochromator detuned to 50% at 7999 eV to minimize harmonic contamination. The X-ray beam was defined to be 1 mm vertically by premonochromator slits. An Oxford Instruments continuous-flow liquid helium CF1208 cryostat was used to maintain a constant temperature of 10 K. Data were measured in transmission mode with three nitrogen-filled ionization chambers, using an Fe foil between the second and third ionization chambers for internal energy calibration. The spectra were calibrated by assigning the first inflection point of the Fe foil spectrum to 7111.2 eV. The data represent an average of two to four scans. The effects of a quartet monochromator glitch were removed from the averaged data by four single point replacements at around k = 11.8, 12.1, 12.3, and 12.6 Å^{-1}.

GNXAS Data Analysis. The following approach was used for the GNXAS analysis of the three iron complexes. The atomic coordinates were input into CRYMOL, and the appropriate cluster was determined. Phase shifts were calculated in PHAGEN using the standard muffin-tin approximation with the entire cluster and up to an energy limit of 70 Ry (950 eV) above the Fe K edge. The muffin-tin radii were chosen by scaling Norman radii of the cluster atoms by a factor of about 0.8 in such a way as to match the nearest neighbor distance. The GNPEAK program was then run to identify and select the relevant peaks in the g_n distribution functions and associate each atom with the appropriate phase shifts. GNXAS calculated the various signals from each g_n contribution. Least-square fits were performed in the subprogram FITHEO on the averaged, energy-calibrated, raw absorption data without prior background subtraction or Fourier filtering. The minimization program uses the MINUIT subroutine of the CERN Library. The residual function is minimized by refining parameters for which specified intervals can be input. The nonstructural parameters, E_0, S_0^2, Γ_c, and E_τ were, as usual, calibrated on model compounds and allowed to vary within narrow intervals, observing if they refined to one of the hard limits.[57,58] The structural parameters varied in the refinements were the distance and the associated bond variance σ_R^2 for each two-atom configuration and the distances, the angle, and the covariance matrix elements for the three-atom configurations (unless stated otherwise). Distances and angles were allowed to vary within a preset range, typically ±0.05 Å and ±5°, respectively. Bond and angle variances and the off-diagonal covariance elements were also allowed to vary in restricted ranges: ±0.005 Å^2, ±50 (deg)^2, and ±0.5, respectively. The results were carefully monitored to ensure that all parameters refined inside the allowed range. The coordination numbers were kept fixed to known values.

Results and Discussion

(a) $Fe(acac)_3$. The GNXAS method was applied to $Fe(acac)_3$ Fe K-edge EXAFS data to determine the feasibility of studying the metrical details of inorganic compounds. The ability of GNXAS to provide an accurate description of the MS contribu-

(63) Lind, M. D.; Hamor, M. J.; Hamor, T. A.; Hoard, J. L. *Inorg. Chem.* **1964**, *3*, 34.

Table 1. Comparison of $Fe(acac)_3$ GNXAS Distance and Angle Fitting Results to Crystallographic Values

structural feature (no. of configurations in complex)	GNXAS distances/angles	GNXAS bond variance (σ_R^2)/ angle variance (σ_θ^2)[a]	crystallographic distances/ angles average [range]
Fe−O (6)	1.99 Å	0.002	1.99 Å [1.99−2.00]
Fe−C_1 (6)	(2.98 Å)[b]		2.95 Å [2.93−2.97]
Fe−C_2 (3)	(3.37 Å)[b]		3.34 Å [3.29−3.43]
Fe−C_3 (6)	(4.34 Å)[b]		4.32 Å [4.30−4.33]
O−C_1 (6)	1.22 Å	0.001	1.26 Å [1.24−1.28]
O−C_2 (6)	2.38 Å	0.006	2.34 Å [2.31−2.39]
O−C_3 (6)	2.38 Å	0.008	2.36 Å [2.34−2.38]
Fe−O−C_1 (6)	134°	1×10^1	128° [128−130]
Fe−O−C_2 (6)	101°	4×10^1	101° [99−103]
Fe−O−C_3 (6)	165°	3×10^1	165° [164−166]
O−Fe−O (6)	89°	6×10^1	91° [87−94]
O−Fe−O (3)	175°	3×10^1	175° [174−176]

[a] Bond and angle variances are reported in $Å^2$ and deg^2, respectively. [b] Values were calculated using the fitted Fe−O bond length, O−C bond length, and Fe−O−C angle.

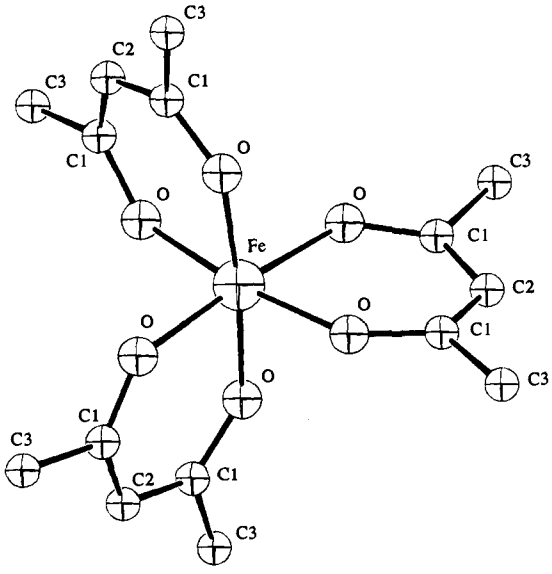

Figure 2. Molecular structure of $Fe(acac)_3$ with atom designations as used in the text.

tions in the EXAFS data of a compound with a noncollinear arrangement of atoms and the reliability of the structural parameters obtained from GNXAS were evaluated. The GNXAS set of programs were used to generate theoretical EXAFS signals corresponding to both two-atom- and three-atom-scattering process. The structure of $Fe(acac)_3$ has been determined by X-ray diffraction.[64] The iron atom is in an octahedral arrangement (Figure 2) surrounded by six oxygen atoms at 1.99 Å, six carbons (C_1) at 2.95 Å, three carbons (C_2) at 3.34 Å, and six carbons (C_3) at 4.32 Å (where the ranges of the distances are given in Table 1). The atomic coordinates of $Fe(acac)_3$ were entered into CRYMOL, and the appropriate cluster (neglecting the hydrogens) was determined (shown in Figure 2). In this case, the cut-off distance was 4.4 Å since the longest Fe−C distance is 4.32 Å and the FT showed no significant features beyond this value. The reduced Norman sphere radii used to calculate the phase shifts were 1.13 Å for Fe, 0.873 Å for O, and 0.899 Å for C. The prototypical two-atom and three-atom configurations (g_2 and g_3 peaks) were identified in the cluster up to 4.4 Å and averaged with a frequency tolerance of 0.1 Å. The resultant coordinates of the atomic configurations were used to calculate the various signals associated with two-atom and three-atom contributions. The signal associated with four two-atom configurations were generated: Fe−O, Fe−C_1, Fe−C_2, and Fe−C_3. Five signals associated with three-atom configurations were calculated: Fe−O−C_1, O−Fe−O (90°), O−Fe−O (180°), Fe−O−C_2, and Fe−O−C_3 (where the three-atom configuration is defined by the two short distances and the intervening angle). The appropriate crystallographic distances and angles for the above mentioned two- and three-atom configurations are listed in Table 1. The fitting program used at the final step of the data analysis built the theoretical absorption spectrum by summing all the two-atom and three-atom contributions. The final spline was in three segments of order 4,4,4 with defining energy points of 7147, 7269, 7577, and 7999 eV. The least-squares fits were done with k^3 weighting over the k range of 2.4−15.1 $Å^{-1}$.

To analyze the MS effects in $Fe(acac)_3$, signals from two-atom configurations were systematically replaced iwth the appropriate three-atom contributions, while monitoring the residual in the EXAFS and the components in the FT. For these fits all the distances and angles were fixed to the crystallographic values while permitting the associated variances and nonstructural parameters to vary. Fit A (Figure 3A) contains only two-atom contributions from Fe−O, Fe−C_1, Fe−C_2, and Fe−C_3. The R value for fit A is 0.181×10^{-4}, and the EXAFS residual clearly contains high-frequency components. In fit A, the first peak of the FT of the data is fit fairly well by the FT of the theoretical signal, but the intensity of the theoretical signal does not match the experimental intensity above 2 Å. The second fit, fit B, includes three-atom signals from Fe−O−C_1, O−Fe−O (90°), and O−Fe−O (180°) while the second and third shells of carbon are still treated as two-atom configurations (Figure 3B). The R value of fit B is 0.635×10^{-5}, almost a factor of 3 better than the R value in fit A, indicating the importance of treating Fe−O−C_1 as a three-atom configuration. Also notice the significant improvement in the fit to the low-k region of the EXAFS, where the Fe−$C_1\gamma^{(2)}$ signal and the Fe−O−$C_1\gamma^{(3)}$ signals differ the most (Figure 4). The contributions from the 90° and 180° O−Fe−O configurations are relatively small as seen by comparison of their amplitudes with the total Fe−O−C_1 signal. The EXAFS residual in fit B still contains some high-frequency components, but the FT of the theoretical signal of fit B begins to match the second peak in the FT of the experimental data at ~2.6 Å. In fit C the second shell of carbons is treated with a three-atom signal. The R value of fit C is 0.553×10^{-5}. Fit C is not a significant improvement over fit B because the signal generated by the Fe−O−C_2 configuration is negligible (Figure 3C). Both the EXAFS data and the FT look very similar to those in fit B. In fit D a signal from Fe−O−C_3 is included. The signal from Fe−O−C_3 is fairly strong, and the R value of fit D decreased to 0.202×10^{-5}. All of the distinguishable regular high-frequency components have been removed in the fit D residual, and the FT of theoretical signals is in very good agreement with the experimental FT up to ~4 Å (Figure 3D). Notice that, even though the Fe−C_3

(64) Iball, J.; Morgan, C. H. *Acta Crystallogr.* **1967**, *23*, 239.

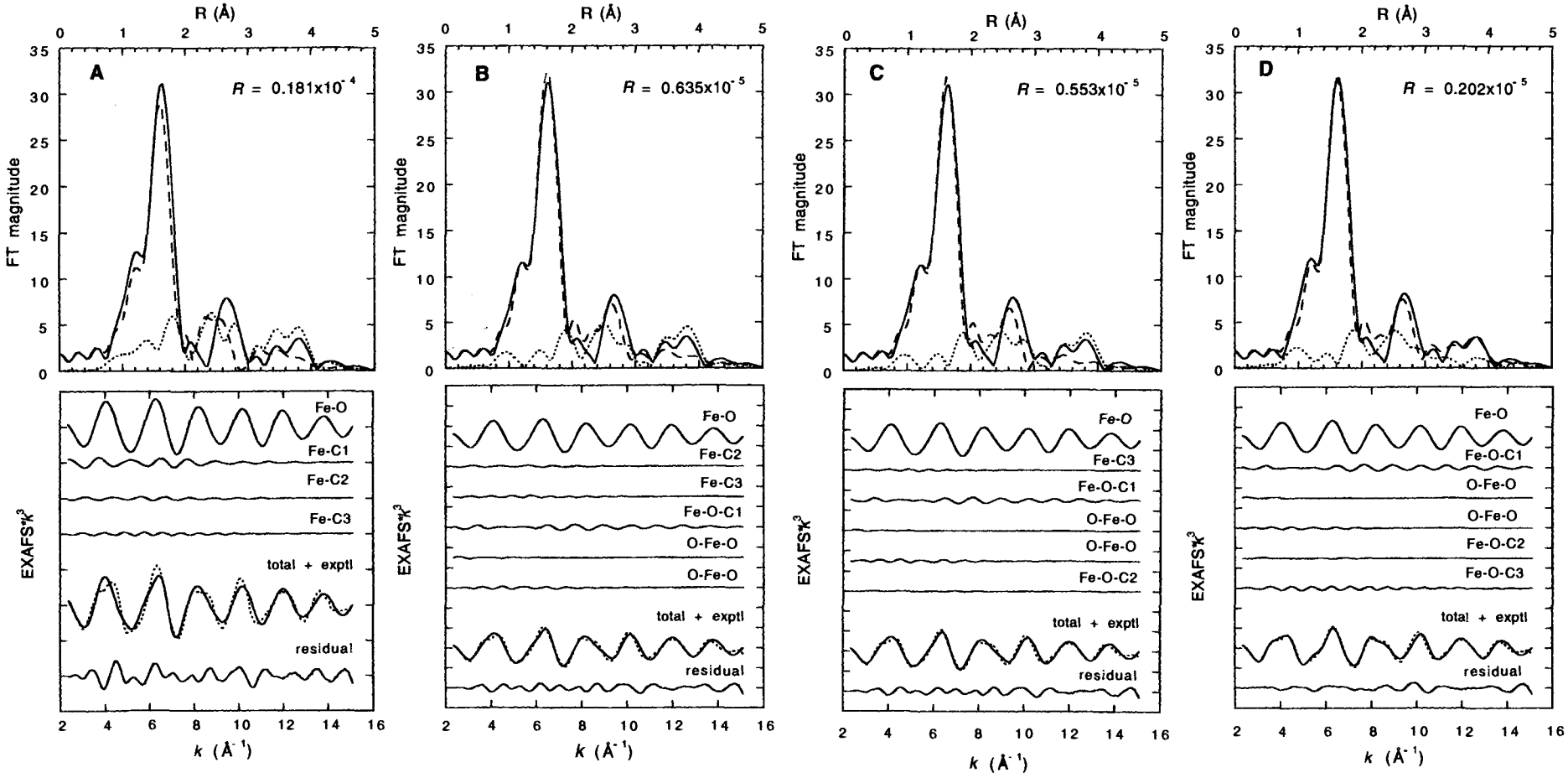

Figure 3. Comparison of the theoretical and experimental signals of the k^3-weighted EXAFS data and the FT of fit A, fit B, fit C, and fit D of $Fe(acac)_3$. The top portion of the figure contains the non-phase-shift-corrected FT of the k^3-weighted EXAFS data of the experimental data (—) and that of the total theoretical signal (- - -). Also shown is the FT of the residual, (•••). The lower portion of the figure presents the EXAFS signals for the individual contributions. The total theoretical signal is also shown (—) and compared with the experimental data (•••) with the residual being the difference between the experimental and the theoretical EXAFS. (The ordinate scale is 10 between two consecutive tick marks.) Fit A contains only $\gamma^{(2)}$ contributions. The residual in fit A contains many high-frequency components, and the fit does not match the data between 2 and 4 Å in the FT. Fit B includes contributions from Fe−O−C_1 and 90° and 180° O−Fe−O configurations. Notice the reduction of the residual in the low-k region of the EXAFS and the improvement of the fit to the FT between 2 and 3 Å. Fit C includes contributions from Fe−O−C_2. There is no noticeable improvement in the fit to the data since the Fe−O−C_2 signal is weak. Fit D includes contributions from Fe−O−C_3. Note the considerable improvement in the fit to the data between 3.5 and 4.1 Å in the FT.

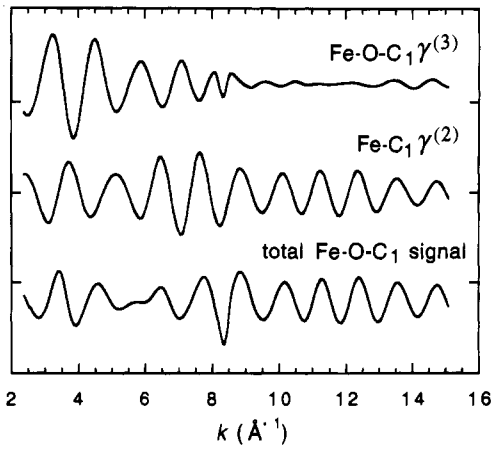

Figure 4. Comparison of the Fe−C_1 $\gamma^{(2)}$ EXAFS signal to the Fe−O−C_1 $\gamma^{(3)}$ signal and the total Fe−O−C_1 signal. The anomalous behavior of the Fe−O−C_1 $\gamma^{(3)}$ signal near 8 Å^{-1} is due to the existence of a deep minimum in the amplitude function of the three-atom signal. Note that the Fe−O−C_1 $\gamma^{(3)}$ signal is out of phase with the Fe−C_1 $\gamma^{(2)}$ signal between 2.5 and 7.5 Å^{-1}. The low-k EXAFS can only be properly accounted for when the first shell of carbons (C_1) is treated in a three-atom configuration (Fe−O−C_1), including both the SS and MS contributions. (The ordinate scale is 5 between two consecutive tick marks.)

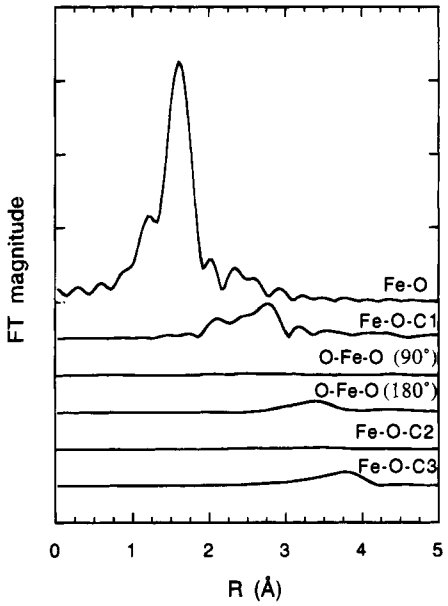

Figure 5. FT of the EXAFS signals of $Fe(acac)_3$ for the individual contributions shown in Figure 3D. This display is a useful way to determine which signals contribute in which regions and shows clearly the significant and complex contributions from Fe−O−C_1 and Fe−O−C_3. (The ordinate scale is 10 between two consecutive tick marks.)

distance is longer than 4 Å, the Fe−O−C_3 signal is significant. This enhancement is in part due to a focusing effect since the Fe−O−C_3 angle is relatively large (165°). Figure 5 displays the individual contributions of each signal in the FT. The dominant feature in the FT is the Fe−O signal with the Fe−O−C_1 and O−Fe−O (180°) and Fe−O−C_3 signals contributing at higher R values.

The ability of the GNXAS method to accurately determine bond distances and angles was also evaluated. Fits were done by varying the distances and angles and applying constraints to keep them within 5% of the crystallographic values. The initial covariance matrix elements were obtained from fit D and were allowed to vary within 10% of those values. A comparison of the crystallographic values with the distances and angles obtained from the best fit to the data is presented in Table 1. The R value of this fit was 0.142×10^{-5} (slightly better than that of fit D), and the bond distances and angles were quite close to the crystallographic values. The fit to the experimental data looks very similar to fit D with a slight improvement of the fit in the Fourier transformed data between 2.5 and 3.0 Å. The bond distances and angles obtained from the GNXAS fit to the experimental data are within the range of the crystallographic values as given in Table 1 with a few exceptions. The values obtained from the Fe−O−C_1 signal deviate from the range of crystallographic values by 0.02 Å for the O−C_1 distance and 4° for the Fe−O−C_1 angle, causing the Fe−C_1 distance to deviate from the crystallographic value by 0.03 Å.

The level of accuracy in this fit indicates that the theory is quite reliable in reproducing the phase of the experimental signal, as has been confirmed by previous experiments.[21-25] Over a large number of fits varying the nonstructural parameters and spline and differing the number of contributions, the Fe−O distance varied by less than 0.01 Å and the Fe−O−C angles by less than 1°, while the O−C_1 distance varied up to 0.04 Å, the O−C_2 distance 0.1 Å, and the O−C_3 distance 0.02 Å. The stronger the signal the smaller the variation in the distance/angle between fits. The amplitude of the signal is determined with slightly less accuracy because amplitudes are affected in the fits by several variables which can be strongly correlated (S_0^2, E_r, Γ_c, bond variances, and the covariance matrix elements). However, the variations of the above-mentioned parameters were confined in narrow ranges determined by physical constraints. In the $Fe(acac)_3$ case, values for the bond variances are not well-known since a theoretical approximation of the molecular vibrations is not available. However, fitted values followed reasonable trends with the Fe−O distance having the lowest variance of all the $\gamma^{(2)}$ contributions in fit A. In a comparison of the variances for the O−C distances, O−C_1 had the lowest variance, O−C_2 had a much higher variance with the static disorder in the O−C_2 distances being over twice that of the O−C_1 distances, and O−C_3 (with C_3 being the carbon in the methyl groups) had the highest mean square deviation.

The EXAFS signal generated by GNXAS matches closely that of the experimental signal of $Fe(acac)_3$ when all the MS contributions were added into the theoretical signal. A comparison of the FT in Figure 3A, where only the two-atom signals were taken into account, with the FT in Figure 3D, where the three-atom signals were also used, shows the importance of including MS contributions from the three shells of carbon atoms. Not only does the GNXAS theoretical fit match the experimental data but the bond distances and angles in the final fit were within 4% of the crystallographic average values with the majority of the bond distances and angles being within the range of the crystallographic values (see Table 1). The number of parameters used in the fit is 18 (two parameters for each bond, the length and its variance, and two for each angle, the angle and its variance, since in this application the off-diagonal elements of the correlation matrix have been fixed to zero) plus three (S_0^2, E_r, and Γ_c), for a total of 21. This number can be compared with the number of independent data points $N_I = (2\ \delta k\ \delta R/\pi) + 2 = 36$, for $\delta k = 12$ Å^{-1} and $\delta R = 4.5$ Å. Notice that the number of neighbors has been fixed and that the two-body parameters are also associated with three-body signals. In this manner, the same parameters can be associated with both a strong and a weak signal. The independent data to parameter ratio determined above show that the fit is overdetermined by nearly a factor of 2, pointing to the reliability of the fit. A point worth mentioning is that the three-atom MS signal from Fe−O−C_1 is out of phase with the Fe−C_1 signal between 2.5 and 7.5 Å^{-1} (the Fe−O−C_1 signal dies off after 7.5 Å^{-1}) (this can be seen in Figure 4). This has implications when

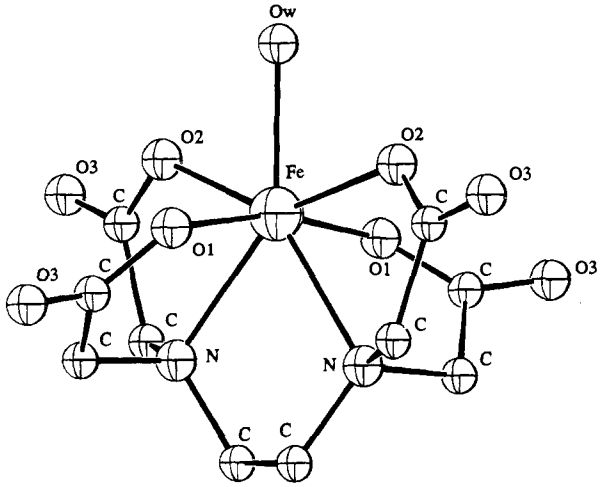

Figure 6. Molecular structure of $[Fe(OH_2)EDTA]^-$ with atom designations as used in the text.

using SS Fe−C second-shell parameters in empirical fits. One can only assume phase and amplitude transferability in the second shell if the two distances and *the angle* of the model are very close to the comparable distances and angle in the unknown. Therefore, the GNXAS method is advantageous in that it can account for the strength and the complexity of MS contributions in an inorganic compound with a noncollinear arrangement of atoms. Once the MS signals are modeled correctly, reliable bond distances and angles can be obtained not only from the first shell but also from second- and third-shell neighbors without dependence on obtaining suitable models from which to extract such empirical parameters.

(b) Na[Fe(OH$_2$)EDTA]. Similar methodology was applied to Na[Fe(OH$_2$)EDTA] Fe K-edge EXAFS data to evaluate the ability of GNXAS to theoretically analyze the EXAFS data of a lower-symmetry coordination complex with mixed ligation. The structure of $[Fe(H_2O)EDTA]^-$ (shown in Figure 6) is not as well-ordered as that of Fe(acac)$_3$ and more like the structures of metalloenzymes for which it is expected that the GNXAS methodology will be particularly useful. The crystal structure of Li[Fe(OH$_2$)EDTA]·2H$_2$O was previously reported.[63] The iron atom is surrounded by five oxygens and two nitrogens in the first shell with two O_1's at 1.97 Å, two O_2's at 2.11 Å, a water at 2.11 Å, and two N's at 2.32 Å. Each oxygen (except for the water) is bound to a carbon which is bound to another oxygen. Each nitrogen is bound to three carbons that link the hexadentate ligand. The crystallographic values of Li[Fe(OH$_2$)EDTA]·2H$_2$O were used to generate the two-atom and three-atom configurations up to 4.5 Å with a frequency tolerance of 0.1 Å. The reduced Norman sphere radii used in the phase shift calculation were 1.17 Å for Fe, 0.730 Å for O, 0.751 Å for N, and 0.772 Å for C. The peaks in the two-atom distribution include two short Fe−O_1 distances, two long Fe−O_2 distances, one Fe−OH_2 distance, two Fe−N distances, 10 Fe−C distances between 2.83 and 3.16 Å, and four Fe−O_3 distances between 3.91 and 4.22 Å. There were approximately 30 unique three-atom contributions which ranged in distance from 3.04 to 4.5 Å. The signals attributed to each of the two- and three-atom configurations were calculated. Due to the complexity of the structure, contributions to the fits were systematically introduced. The spline was in three segments of order 3, 4, 4 with defining energy points of 7155, 7250, 7600, and 7999 eV. Least-squares fits were done with k^3 weighting over the k range 2.8−15.1 Å^{-1}.

The first-shell fit contained waves from the following two-atom configurations: Fe−O_1 [2] at 1.97 Å, Fe−O_2 [3] at 2.11 Å, and Fe−N [2] at 2.32 Å, where the number in the brackets

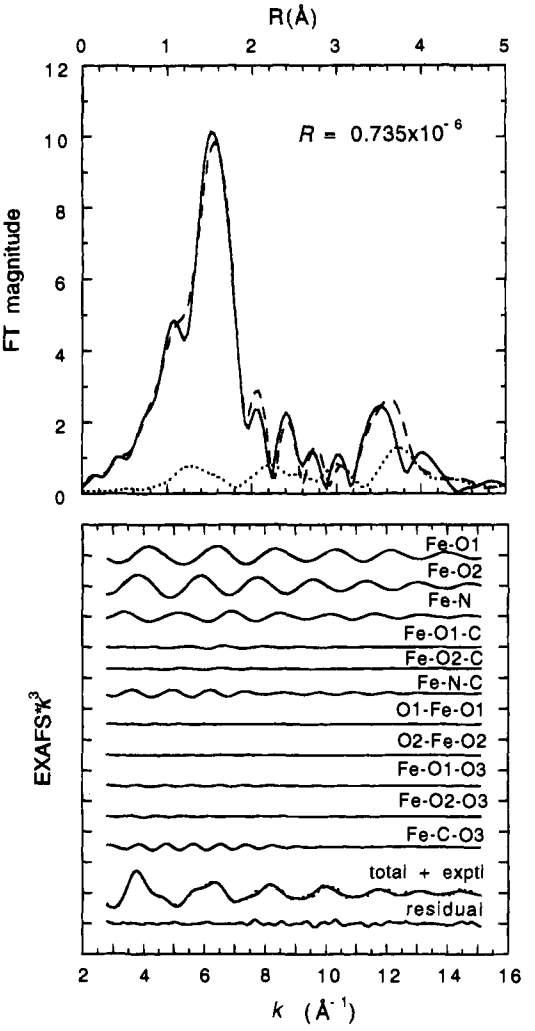

Figure 7. Comparison of the GNXAS theoretical signal with experimental data of Fe K-edge k^3-weighted EXAFS data between 7155 and 7999 eV of Na[Fe(OH$_2$)EDTA]. The top portion of the figure contains the non-phase-shift-corrected FT of the k^3-weighted experimental EXAFS data (—) and that of the total theoretical signal (- - -). Also shown is the FT of the residual (•••). The lower portion of the figure presents the EXAFS signals for the individual contributions. The total theoretical signal is also shown (—) and compared with the experimental data (•••) with the residual being the difference between the experimental and the theoretical EXAFS. (The ordinate scale is 10 between two consecutive tick marks.)

indicates the coordination number (see Table 2 for the range of crystallographic distances). The Fe−OH_2 and long Fe−O_2 distances were treated together since they both have a distance of 2.11 Å. All five oxygens could not be averaged and treated as a single shell because the EXAFS signals from the short Fe−O_1 and longer Fe−O_2 strongly interfere at higher k (Figure 7). This first-shell fit (not shown) gave an R value of 0.118×10^{-4} with good agreement between the FT of the experimental data and the fit signal up to 2.0 Å (corresponding to ~2.4 Å in the cluster when the phase shift is taken into account). The major contributions in the EXAFS signal were accounted for using the three first-shell distances, with especially good agreement at higher k. The next fit included signals from three-atom configurations: Fe−O_1−C, Fe−O_2−C, and Fe−N−C. The R value decreased to 0.437×10^{-5}. The total theoretical EXAFS signal fits extremely well to the experimental EXAFS above $k = 8$ Å^{-1}, and there were several peaks between 2.0 and 3.0 Å in the FT. However, peaks above 3.0 Å in the FT were not being fit well and high-frequency components could be seen in the EXAFS residual, especially at lower k. Therefore other three-

Table 2. Comparison of the Na[Fe(OH_2)EDTA] GNXAS Values to the Crystallographic Values of Li[Fe(OH_2)EDTA]·$2H_2O$

structural feature (no. of configurations in complex)	Na[Fe(OH_2)EDTA] GNXAS distances/angles	Na[Fe(OH_2)EDTA] GNXAS bond variance (σ_R^2)/ angle variance (σ_θ^2)[a]	Li[Fe(OH_2)EDTA]·$2H_2O$ crystallographic distances/ angles average [range]
Fe−O_1 (2)	1.97 Å	0.003	1.97 Å [1.94−2.00]
Fe−O_2 (3)	2.10 Å	0.004	2.11 Å [2.11−2.13]
Fe−N (2)	2.33 Å	0.003	2.32 Å [2.30−2.35]
O_1−C (2)	1.33 Å	0.005	1.28 Å [1.27−1.29]
O_2−C (2)	1.30 Å	0.004	1.26 Å [1.26−1.27]
N−C (6)	1.48 Å	0.002	1.47 Å [1.47−1.48]
$O_{1,2}$−O_3 (4)	2.30 Å	0.006	2.23 Å [2.20−2.25]
C−O_3 (4)	1.27 Å	0.006	1.23 Å [1.21−1.25]
Fe−C (4)	2.91 Å	0.008	2.91 Å [2.79−2.99]
Fe−O_1−C (2)	121°	3×10^1	120° [119−121]
Fe−O_2−C (2)	119°	6×10^1	122° [121−123]
Fe−N−C (6)	106°	1×10^1	108° [103−112]
O_1−Fe−O_1 (1)	170°	1×10^1	166°
O_2−Fe−O_2 (1)	150°	2×10^0	145°
Fe−O_1−O_3 (2)	150°	5×10^1	145° [142−148]
Fe−O_2−O_3 (2)	155°	5×10^1	149° [148−150]
Fe−C−O_3 (4)	158°	1×10^1	158° [153−161]

[a] Bond and angle variances are reported in $Å^2$ and deg^2, respectively.

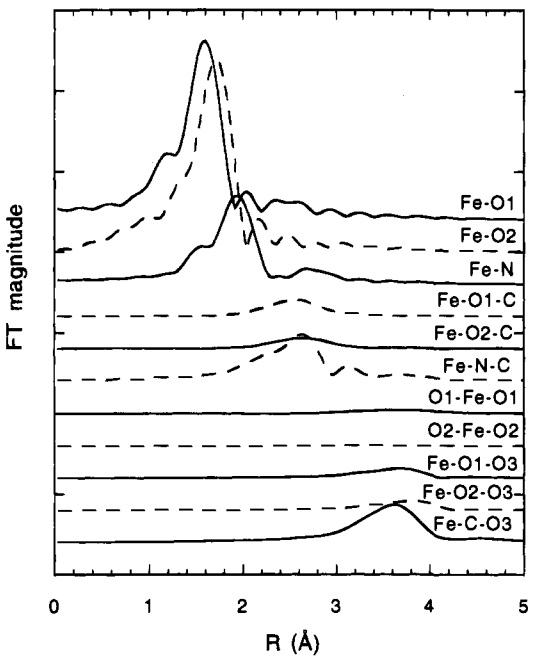

Figure 8. FT of the EXAFS signals of Na[Fe(OH_2)EDTA] for the individual contributions shown in Figure 7. The first-shell signals contribute signicantly below 2.5 Å with the Fe−O_1−C, Fe−O_2−C, and Fe−N−C signals contributing between 2.5 and 3.2 Å. The main contribution above 3.0 Å comes from Fe−C−O_3. (The ordinate is 5 between two consecutive tick marks.)

atom components were examined for signals that were relatively strong and of the same frequency as those in the residual.

All the ~90° signals associated with O−Fe−O, O−Fe−N, and N−Fe−N were extremely weak. Both the O_1−Fe−O_1 and O_2−Fe−O_2 MS signals contributed only a small amount at low k. The Fe−O_1−O_3 and Fe−O_2−O_3 signals were significant. However, the Fe−C−O_3 contributions was found to be extremely strong and largely responsible for the peak in the FT at ~3.5 Å. The best fit was obtained when the last five mentioned contributions were included. The results of this fit are shown in Figure 7, and a comparison of the distances and angles to the Li[Fe(OH_2)EDTA]·$2H_2O$ crystallographic values are given in Table 2. The individual contributions to the FT are shown in Figure 8. With an R value of 0.735×10^{-6}, this fit was a factor of 6 better than the fit that included the first neighbors and Fe−O_1−C, Fe−O_2−C, and Fe−N−C signals. The fit compares extremely well to the experimental EXAFS with the exception of high-frequency components between 7.5 and 12 $Å^{-1}$ (see results in Figure 7). These higher frequency components can possibly be attributed to intermolecular signals that were not accounted for because the cluster was only generated up to 4.5 Å. The FT of the theoretical fit is in close agreement with the FT of the experimental data up to 4.0 Å. The low-frequency EXAFS is dominated by three waves from the g_2 contributions: Fe−O_1, Fe−O_2, and Fe−N. The EXAFS distances for these three shells show excellent agreement with the Li[Fe(OH_2)EDTA]·$2H_2O$ crystallographic values, deviating by <0.01 Å. The Fe−O_1−C, Fe−O_2−C, and Fe−N−C waves have significant contributions in the FT region between 2.0 and 3.0 Å, with Fe−N−C having the largest signal because of the 6-fold degeneracy. The higher frequency region is dominated by the Fe−C−O_3 signal. A focusing effect occurs because of the large Fe−C−O_3 angle (161°).

Not only are the structural values obtained from the GNXAS fit consistent with the crystallographic values but the GNXAS total EXAFS signal compared to the data and the respective FT of the fit and the data agree remarkably well for a low-symmetry coordination complex with mixed ligation. The fitted parameters are in substantially good agreement with crystallographic data, even though the fit is slightly underdetermined (37 fitting parameters compared to 36 independent points). The bond distances obtained from GNXAS for the three first neighbors distance are all within 0.01 Å of the crystallographic values (see Table 2). The GNXAS bond distances and angles that make up the g_3 contributions are within 4% of the average crystallographic values, with the strength of the signal influencing the goodness of the match. The configurations with stronger signals have distances and angles that are closer to the crystallographic values than the configurations with weaker signals. For example, the first shell has the strongest contributions and the calculated distances are within the range of the Li[Fe(OH_2)EDTA]·$2H_2O$ crystallographic values. The Fe−N−C signal is much stronger than the Fe−O−C signals. The difference between the crystallographic and calculated N−C distance is 0.01 Å while the difference between the crystallographic and calculated O−C distance is 0.05 Å. Since the Fe−C−O_3 signal is strong, accurate distances and angles are obtainable, even though the O_3 atoms are over 4 Å away from the Fe atom. GNXAS also proved to be internally consistent, in that the first-shell distances varied <0.01 Å, the low-Z bond distances (*i.e.*, O−C and N−C) varied ±0.04 Å, and the bond angles varied ±3° over a large number of fits with varying contributions, splines, and nonstructural parameters.

(c) $K_3Fe(CN)_6$. The GNXAS programs were applied to $K_3Fe(CN)_6$ EXAFS data to investigate the MS of the linear Fe−C−N unit and to test the feasibility of using GNXAS for angle determination studies for low-Z diatomics coordinated to transition metal centers. The iron atom in $K_3Fe(CN)_6$ is in an octahedral environment[65] with an average Fe−C bond distance of 1.94 Å and a range of 1.93−1.94 Å. The Fe−C−N angle ranges from 177 to 179° with a C−N distance of 1.15 Å. The crystallographic values of $K_3Fe(CN)_6$ were used to characterize the two-atom and three-atom configurations up to 4.5 Å with a frequency tolerance of 0.1 Å. The reduced Norman sphere radii used in the phase shift calculation were 0.946 Å for Fe, 0.654 Å for C, and 0.668 Å for N. The two-atom configurations included Fe−C while the three-atom configurations included Fe−C−N, C−Fe−C (90°), and C−Fe−C (180°). The two-region spline had orders of 3, 4 with defining energy points of 7160, 7300, and 7999 eV. The coordination numbers were fixed to the known values, and the Fe−C and C−N distances were allowed to vary along with the respective variances. The independent points to parameters ratio is 36 to 19, indicating that the fit to the data will be overdetermined by almost a factor of 2. A comment has to be made for collinear configurations. In the GNXAS programs, a Taylor expansion of amplitudes and phases is used during the fitting procedure with first-order derivatives. For a collinear structure ($\theta = 180°$), the first-order derivative is zero and therefore the program uses the second derivative. Thus, the thermal and configurational averages of the Fe−C−N contributions were performed using a second-order Taylor expansion for the amplitude and phase around $\theta = 180°$, as described elsewhere.[9] The agreement with the experimental data was found to be much worse with fits having angles $\theta < 178°$, thus indicating a strong sensitivity of the signal to the geometry of the collinear configuration. In addition, the angles around the iron were constrained to be octahedral. Least-squares fits were done with k^3 weighting over the k range 2.9−15.1 $Å^{-1}$.

The best fit gave an Fe−C distance of 1.92 Å and a C−N distance of 1.18 Å. The EXAFS contributions and the FT of the best fit are presented in Figure 9 and show good agreement to the experimental data. The Fe−C SS signal and the Fe−C−N MS signal dominate the EXAFS spectrum. The angular sensitivity of the Fe−C−N signal was investigated by fixing all the distances and variances and generating the MS signal from Fe−C−N and the SS signal from Fe−N as a function of the Fe−C−N angle (Figure 10). The MS signal from the Fe−C−N unit shows considerable amplitude enhancement for angles greater than about 150°, as reported in earlier papers for Fe−O−Fe and metal carbonyl systems.[8-12] This indicates that GNXAS can be used to analyze MS effects as a function of angle, and where the angular dependent amplitude/phase effects become significant (above about 150°), angles can be fairly accurately determined for Fe−C−N configurations. This should also be the case for similar systems such as nitrosyl and dioxygen complexes even when contributions from other outer shell scatterers may be present.

Summary

In this paper an *ab-initio*, integrated approach to EXAFS data analysis, called GNXAS, has been described in detail. The characteristics and advantages of this approach were investigated by applying the method to Fe K-edge EXAFS data of three iron coordination complexes of known structure. Accurate structural results were obtained by using a fitting procedure which takes into account two-atom and three-atom MS signals.

(65) Figgis, B. N.; Skelton, B. W.; White, A. H. *Aust. J. Chem.* **1978**, *31*, 1195.

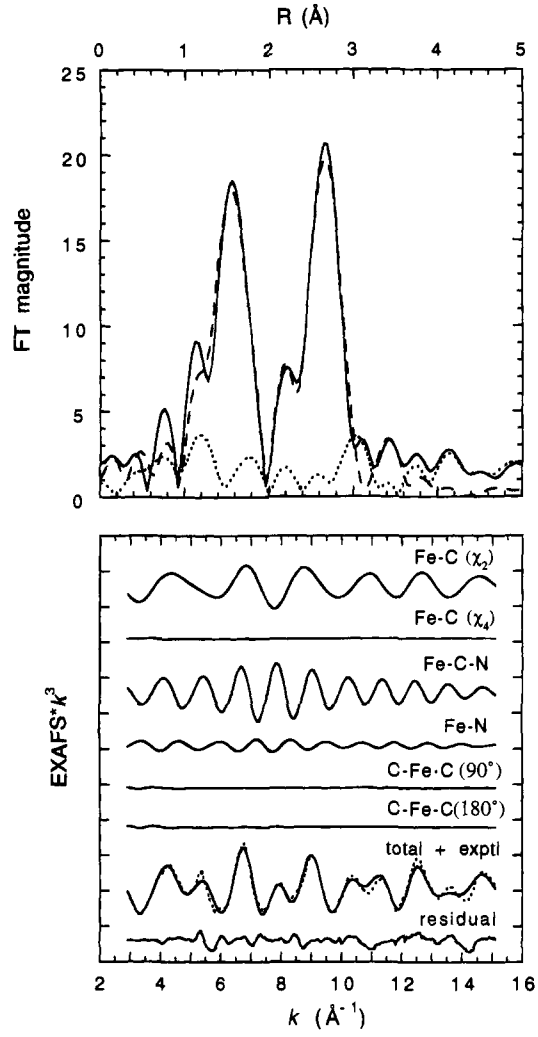

Figure 9. Comparison of the GNXAS theoretical signal with experimental data of Fe K-edge k^3-weighted EXAFS data between 7160 and 7999 eV of $K_3Fe(CN)_6$. The top portion of the figure contains the non-phase-shift-corrected FT of the k^3-weighted experimental EXAFS data (—) and that of the total theoretical signal (- - -). Also shown is the FT of the residual (•••). The lower portion of the figure presents the EXAFS signals for the individual contributions. The total theoretical signal is also shown (—) and compared with the experimental data (•••) with the residual being the difference between the experimental and the theoretical EXAFS. (The ordinate scale is 10 between two consecutive tick marks.) The two major contributions to the EXAFS signal are the SS signal from Fe−C and the MS signal from the linear Fe−C−N.

The raw data were fit in a way that reduces the tedious standard preanalysis of manual spline−background removal and without dependence on obtaining suitable models from which to extract empirical phase and amplitude parameters. First neighbor distances deviated less than 0.01 Å from the crystallographic values, which is comparable or better than that which can be obtained by empirical-based methods. Bond distances and angles of second (and in some cases third) neighbors were also obtained due to the accurate modeling of MS contributions. The second and third neighbor distances and angles were found to be in good agreement with crystallographic values, typically within the crystallographic range and varying only 4% in distance and angle from the average. These findings are of general importance for structural studies of chemical systems, including inorganic complexes and metalloproteins. Further, they demonstrate that a proper treatment of the MS components in the EXAFS signal is necessary to get reliable structural information on distant neighbors. Moreover, accurate bond angle determination for angles over about 150° is feasible for

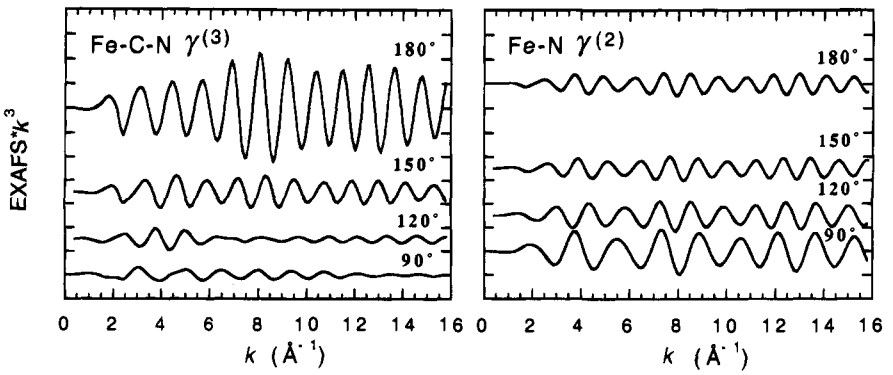

Figure 10. Comparison of the EXAFS signals of the $\gamma^{(3)}$ Fe−C−N contribution to the $\gamma^{(2)}$ Fe−N contribution when the Fe−C−N angle equals 180°, 150°, 120°, and 90°. Notice the increased amplitude enhancement of the $\gamma^{(3)}$ Fe−C−N signal above 150°. This indicates that GNXAS can be used to determine angles fairly accurately above 150° for Fe−C−N configurations and other similar systems where diatomics may be coordinated to a transition metal center. (The ordinate scale is 10 between two consecutive tick marks.)

Fe−C−N and other similar systems using the GNXAS approach to accurately analyze MS effects.

Acknowledgment. This research was supported by grants from the NSF (CHE91-21576, K.O.H.) and NIH (RR01209, K.O.H.; GM40392, E.I.S.) and also the Italian INFN and CNR research institutions. Stanford Synchrotron Radiation Laboratory is supported by the Department of Energy, Office of Basic Energy Science, Divisions of Chemical Science and Material Science, and in part by the National Institutes of Health, National Center of Research Resources, Biomedical Research Technology Program (RR-01209), and DOE's Office of Health and Environmental Research.

Appendix

A more rigorous discussion of the MS formalism is provided here to further expand the theoretical basis behind GNXAS. It is convenient to start with the derivation of the photoabsorption cross section. In the framework of MS theory, the amplitude for each possible path that begins and ends at the photoabsorber has to be obtained. These amplitudes must then be summed and multiplied by the amplitude M_l for the creation of the photoelectron. Then, the imaginary part must be taken (which, as discussed below, is equivalent to taking the modulus square).

The propagation amplitude can be described by remembering that a spherical wave of angular momentum $L = (l, m)$ around a center i scattering off an atom located at that center is multiplied by

$$t_l^i = \exp(i\delta_l^i)\sin(\delta_l^i) \tag{A1}$$

where δ_l^i is the phase shift experienced by the electronic wave in traversing the atomic spherical potential (which conserves l). Moreover the propagation from atom i to atom j is free and is described by the amplitude $G_{LL'}^{ij}$, where L and L' represent the angular momenta around sites i and j, respectively. The explicit expression will be given below. Since there cannot be self-propagation, $i \neq j$ and $G_{LL'}^{ii} = 0$.

The amplitude of the path that goes from the photoabsorber (assumed located at site o), around which the photoelectron has angular momenta l and m determined by the polarization of the photon, to a neighboring atom (located at any site j), where it can arrive with any angular momentum (one has to sum over all possibilities) and then returns to the photoabsorber with the same starting angular momentum, is then given by

$$\sum_{jL'} t_l^o G_{lm,L}^{oj} t_{l'}^j G_{L',lm}^{jo} t_l^o \tag{A2}$$

This is the so-called SS contribution. Similarly the contribution from a double-scattering process involving sites i and j is found to be

$$\sum_{ijL'L''} t_l^o G_{lm,L}^{oi} t_{l'}^i G_{L',L''}^{ij} t_{l''}^j G_{L'',lm}^{jo} t_l^o \tag{A3}$$

From these expressions, the intermediate summations over sites and angular momenta can be viewed as matrix products between the matrix $G_{LL'}^{ij}$ and the matrix

$$(T_a)_{LL'}^{ij} = \delta_{ij}\delta_{LL'}t_l^i = \delta_{ij}\delta_{LL'}\exp(i\delta_l^i)\sin(\delta_l^i) \tag{A4}$$

The matrix is diagonal in the site and angular momenta indices and contains all the dynamical information of the interaction between electrons and atoms of the system. The structural information is contained in the propagators $G_{LL'}^{ij}$ (called structure factors). The separation property between structure and dynamics is maintained even if the muffin-tin approximation is abandoned and the regions around the atoms are not spheres but polyhedra (*i.e.*, leaving no interstitial space). The only change in this latter case is that the atomic matrix element t_l^i is no longer diagonal in the angular momentum and depends on the azimuthal quantum number m: $t_l^i \rightarrow t_{LL'}^i$ so that $(T_a)_{LL'}^{ij} = \delta_{ij}t_{LL'}^i$.

Thus, any scattering contribution of order $n - 1$ is given by the matrix element (notice that the term $n = 1$ is zero)

$$[(T_aG)^nT_a]_{lm,lm}^{oo} \tag{A5}$$

All possible contributions to the cross section are given by

$$\sum_{n=0}^{\infty} M_l[(T_aG)^nT_a]_{lm,lm}^{oo} \tag{A6}$$

In this equation the matrix element is multiplied by the amplitude M_l for the creation of the photoelectron in the $l = 1$ final state to get the complete amplitude of the photoabsorption process (creation plus propagation back to the photoabsorber). Notice that the $n = 0$ term represents the atomic photoabsorption. The modulus square of this quantity is proportional to the photoabsorption cross section. For real potentials, a generalized optical theorem relates the square of the scattering amplitude to its imaginary part. This theorem can be checked for the atomic absorption remembering eq A1, whereby

$$|M_lt_l^o|^2 = M_l^2(\sin\delta_l^o)^2 = M_l^2\mathcal{T}t_l^o \tag{A7}$$

and can be applied generally to the complete amplitude.[45]

By inserting the proper factors and summing over the final azimuthal m values, the unpolarized one-electron absorption cross section from a cluster of atoms is

$$\sigma_e(E) = \frac{8}{3}\pi^2\alpha\omega\mathcal{T}\sum_{n=0}^{\infty}\frac{1}{(2l+1)}\sum_m M_l^2[(T_aG)^nT_a]_{lm,lm}^{oo} \quad (A8)$$

where α is the fine structure constant ($\alpha = 1/137$) and ω is the photon energy ($\omega = I_c + E$). Equation A8 can also be written as

$$\sigma_e(E) = \sigma_0(E)[1 + \chi(E)] \quad (A9)$$

where $\sigma_0(E)$ is the atomic absorption cross section and is given by

$$\sigma_0(E) = \frac{8}{3}\pi\alpha\omega M_l^2 \sin^2\delta_l^o = \frac{8}{3}\pi\alpha\omega M_l^2\mathcal{T}t_l^o \quad (A10)$$

and the structural contribution to the cross section describing the interference processes is

$$1 + \chi(E) = \frac{1}{\mathcal{T}t_l^o}\frac{1}{(2l+1)}\mathcal{T}\sum_m[(I - T_aG)^{-1}T_a]_{lm,lm}^{oo} \quad (A11)$$

Notice that in this last equation we have summed the geometrical series

$$\sum_{n=0}^{\infty}(T_aG)^nT_a = (I - T_aG)^{-1}T_a \quad (A12)$$

By inverting the MS matrix ($I - T_aG$), all the scattering contributions to the cross section can be obtained. The mathematical conditions under which eq A12 is valid are discussed in refs 37 and 45. Equation A11 is the general result valid in all the photoelectron energy range. For pedagogical reasons, we have adopted the reverse path of going from the series to the exact MS matrix inversion. There are now contentions[18] that eq A12 holds for all energies when the proper configurational averages over the thermal (and structural) disorder are taken. In any case, the complete matrix inversion can still be performed as a means for calculating all the MS contributions relating to a subset of all the atomic sites, those instances where the series might converge too slowly for the summation to be carried term by term (*vide infra*).

Two more comments are in order. In all the above formulas a real potential has been implicitly assumed, especially for writing eq A7. However, providing that the square of the atomic dipole matrix element M_l^2 is replaced by $|M_l|^2$ and $\mathcal{T}t_l^o$ is used instead of $\sin^2\delta_l^o$, the same formulas are approximately valid for a complex potential. Secondly, the formulas derived are valid for any initial state l_i, provided the transition to the $l_i - 1$ state is neglected compared to the $l_i + 1$ transition, an approximation which is nearly always justified. For more details on these two points and general exact formulas, see refs 37 and 45.

From the expression A11 for the structural contribution describing the modulations of the absorption cross section, the only components needed are the atomic matrix elements t_l^i for all atomic sites i and all angular momenta up to an l_{max}. According to scattering theory,[66] l_{max} is given by $l_{max} = kR_{mt}$, where k is the photoelectron wave vector and R_{mt} is the muffin-tin radius of the atom at site i, and the structure factors $G_{LL'}^{ij}$ describing the propagation of spherical waves.

The atomic matrix elements are given by

$$t_l^i = \left.\frac{W[j_l(\kappa r_i),R_l^i(r_i)]}{W[-ih_l^+(\kappa r_i),R_l^i(r_i)]}\right|_{r_i=R_{mt}} \quad (A13)$$

where $W[f(r),g(r)] = f(r)\,g'(r) - g(r)\,f'(r)$ is the Wronskian between the functions f and g, $j_l(kr)$ and $h_l^+(kr)$ are spherical Bessel and Hankel functions, respectively, and $R_l^i(r)$ is the solution of the radial Schrödinger equation with angular momentum l and a complex effective potential for the atom at site i that is regular at the origin. The internal momentum κ is given by $\kappa = (E - \bar{V}_0)^{1/2}$, where $\bar{V}_0$ is the internal (complex) interstitial potential. The subscript in the radial coordinate r_i means that it is referred to the origin of the atom sitting at site i while the Wronskian is calculated at the muffin-tin radius R_{mt} of the atom. The quantities $t_l^i(E)$ are obtained and stored as a function of site, angular momentum, and energy.

The structure factors have a more complicated expression, making the evaluation of the MS terms rather laborious (this was one of the motivations to seek simpler approximate expressions). The structure factors are given by

$$G_{LL'}^{ij} = 4\pi i\sum_{L''} i^{l+l''-l'}C_{LL''}^{L'}\,h_{l''}^+(\kappa R_{ij})\,Y_{L''}(\hat{R}_{ij}) \quad (A14)$$

where the quantities $C_{LL''}^{L'}$ are the Gaunt Coefficients given by

$$C_{LL''}^{L'} = \int d\Omega\, Y_L^*(\Omega)\,Y_{L'}(\Omega)\,Y_{L''}(\Omega) \quad (A15)$$

and l and l' go up to l_{max}.

By using these two equations, the theoretical model signal needed for the analysis of the experimental data can be calculated. However, even though eq A11 is capable of generating the total signal relating to the whole cluster probed by the photoelectron, it is not used for data analysis because of physical and computational reasons. Computationally the storage and the inversion of a complex, usually double-precision, matrix having dimensions $N \times N$, where $N = N_{at}(l_{max} + 1)^2$, N_{at} being the number of atom in the cluster, is not trivial, since N_{at} might be on the order of 20 or more with $15 \le l_{max} \le 20$ for ordinary spectra up to $k \approx 15$ Å. Since the time needed for inverting a matrix of dimensions $N \times N$ goes as N^3, the fitting of theoretical signals calculated by this method onto the experimental data is not practically viable if the input structural parameters are varied, not to mention the possibility of doing configurational averages. The physical reason is that a relatively limited number of paths is usually responsible for the observed modulations of the absorption coefficient. This fact, even though it constitutes a limitation on the informational content of the physical spectra, provides nonetheless a more analytical insight into the structural problem under investigation and certainly makes it easier to perform configurational averages. This point is also supported by the structure of the MS series in eq A6, which has the appearance of a geometrical series where each term is smaller than the preceding one by a factor $|tG|$. One would be led to think that each additional scattering gives a contribution that is down on average by a factor of $0.2/(\kappa R)$, since $|t|$ is on the order of 0.1~0.2 (apart for particular energy and l values where it can assume its maximum value of 1) and $|G|$ (see below) goes down as $1/(\kappa R)$, where R is the smallest atomic distance in the cluster. This is generally true for paths where there is no constructive interference of all the partial waves intervening in the matrix multiplication T_aG. An exact indicator of the convergence of the MS series would be $\varrho(T_aG)$,[37,45] the modulus of the maximum eigenvalues of the matrix T_aG, but again this is a rather abstract criterium and does not shed light onto the underlying physics of the propagation process of the photoelectron. To obtain more physical insight a reasonably simple approximation for the propagator $G_{LL'}^{ij}$ has to be obtained. It turns out that an accurate high-energy approximation for $G_{LL'}^{ij}$ and one that is quite good at all energies for nearly collinear paths[33,67] is given by

(66) Taylor, J. R. *Scattering Theory*; John Wiley & Sons: New York, 1972.

$$G^{ij}_{LL'} = -i^{l-l'} 4\pi \frac{\exp(i\kappa R_{ij})}{\kappa R_{ij}} c_l(\kappa R_{ij})\, c_{l'}(\kappa R_{ij})\, Y^*_L(\hat{R}_{ij})\, Y_{L'}(\hat{R}_{ij}) \tag{A16}$$

where $\vec{R}_{ij}$ is the vector joining sites i and j, directed from j to i. This expression can be used at all energies and for all paths to make order of magnitude estimates for the contribution of individual paths.

The expression of $c_l(\varrho)$ can be obtained efficiently by the Bessel function recurrence relation

$$c_{l+1}(\varrho) = c_{l-1}(\varrho) + (2l+1)\frac{i}{\varrho} c_l(\varrho) \tag{A17}$$

for $l > 1$, and with starting values

$$c_0(\varrho) = 1 \quad \text{and} \quad c_1(\varrho) = 1 + \frac{i}{\varrho} \tag{A18}$$

The asymptotic expression, always valid in the physical regime for all energies, is given by

$$c_l(\varrho) \cong \exp[il(l+1)/(2\varrho)][1 + l(l+1)/(2\varrho^2)]^{1/2} \tag{A19}$$

Using eq A16 an expression for any MS contribution can be obtained. As a way of illustration the following double-scattering contribution is described. The path described goes from the photoabsorber located at the origin o to an atom located at site j, stopping only once at an intermediate atom at site i. The key to the simplification is the application of the spherical harmonics addition theorem in the intermediate summations over the azimuthal quantum numbers in the matrix multiplication $T_a G$

$$\frac{2l+1}{4\pi} P_l(\hat{R}_1 \cdot \hat{R}_2) = \sum_m Y^*_{lm}(\hat{R}_1)\, Y_{lm}(\hat{R}_2) \tag{A20}$$

where $P_l(x)$ is the Legendre polynomial of order l. For the path contribution

$$\chi^l_3(k) = \frac{1}{\mathcal{T}^o_l} \frac{1}{2l+1} \mathcal{T}\left(t^o_l \sum_{m,m',m''} G^{oi}_{lm,l'm'} t^i_{l'} G^{ij}_{l'm',l''m''} t^j_{l''} G^{jo}_{l''m'',lm} t^o_l \right) \tag{A21}$$

This equation can be rewritten as

$$\chi^l_3(k) = \mathcal{T}\left[\exp(2i\delta^o_l)\, P_l(\hat{R}_{oi} \cdot \hat{R}_{jo})\, c_l(\kappa R_{oi})\, c_l(\kappa R_{jo}) \times \frac{\exp\{i\kappa(R_{oi} + R_{ij} + R_{jo})\}}{\kappa R_{oi} \kappa R_{ij} \kappa R_{jo}} f^i(\hat{R}_{oi} \cdot \hat{R}_{ij};\, R_{oi}, R_{ij})\, f^j(\hat{R}_{ij} \cdot \hat{R}_{jo};\, R_{ij}, R_{jo}) \right] \tag{A22}$$

where the effective curved wave electron scattering amplitude is defined as

$$f^i(\hat{R}_{oi} \cdot \hat{R}_{ij};\, R_{oi}, R_{ij}) = \sum_l (2l+1) t^i_l P_l(\hat{R}_{oi} \cdot \hat{R}_{ij})\, c_l(\kappa R_{oi})\, c_l(\kappa R_{ij}) \tag{A23}$$

As similar equation can be written for f^j. This curved wave scattering amplitude differs from the usual plane wave by the presence of the factor $c_l(\kappa R_{oi})\, c_l(\kappa R_{ij})$, which indeed takes into account the curvature of the spherical electron wave propagating through the system. This factor is essential for a correct description of the electron propagation in the medium and failure to recognize this fact, as done in the plane-wave approximation, has been one of the earlier limitations of EXAFS theories. From the expression A22, it is clear that the functional form of the general contribution χ^l_n is the one given by eq 5.

It is clear from eq A22 that the actual expansion parameter in the MS series is not $|t/\kappa R|$, but in fact $|f/\kappa R|$. Therefore, the behavior of f as a function of the scattering angle $\hat{R}_1 \cdot \hat{R}_2 = \cos\theta_{12}$ must be known in order to obtain the rate of convergence of the series. A plot of this quantity, as shown in Figure 1 of the paper, reveals that $|f(\theta)|$ is sharply peaked in the forward direction ($\theta = 0$). The function is on the order of unity when $\theta = 0$ and then decreases rapidly beyond an aperture cone on the order of ~20° toward a nearly constant value of the order of $|t|$. The mathematical reason for this behavior is that in the forward direction ($\cos\theta = 1$) the Legendre polynomial is a constant independent of $l (P_l(1) = 1)$. There is maximum coherence of all the partial waves, and the resulting interference is constructive, whereas away from this direction the interference begins to be destructive, finally reducing the value of the sum to that of the single term. The destructive interference is particularly effective in the backward direction ($\cos\theta = -1$) where $P_l(-1) = (-1)^l$. Physically this constructive behavior is known as a focusing effect since the atom acts as a focusing lens for the incoming electron. The details of this behavior are clearly dependent on the energy, as is the ratio between the probabilities of forward scattering *vs* scattering in other directions, but it remains valid even if one uses the exact expression for the spherical wave propagators in eq A14. Actually, it is possible to generalize the separable approximation given in eq A16[67] to an almost exact result. With a suitable generalization of the effective scattering factors f, the argument about the expansion parameter and the expression for the contribution of the general MS term as given in eq A22 can still be used.

From the preceding discussion it is clear that when sites o, i, and j are collinear or nearly collinear (within the aperture cone of f), the MS contribution given by eq A22 is quite sizable, especially with respect to what one would expect on the basis of the naive argument that any additional scattering reduces the contribution by a factor $|t/\kappa R|$. Moreover the next order term where the electron scatters off the atom at site i twice (always assuming that the atom at site j is the furthest away) is roughly twice as big as the one just discussed. Therefore, collinear or nearly collinear configurations should be treated to all orders in the forward scattering. At low energies (between roughly 40 and 200 eV depending on the actual system under consideration), backscattering amplitudes are quite sizable even with respect to forward scattering and so paths including more than one such scattering can be important. However the total length of the path has to be considered. It can be shown, from a WKB approximation of the phase shifts, that each path is damped by a factor like the one given by eq 6. Therefore, the longer the path, the more heavily it is damped. Besides, the damping is higher at lower energies and lower at higher energies whereas the scattering factor $f(\theta)$ decreases with increasing energy at all angles, apart from the forward cone. This is due to the fact that the HL potential follows approximately the universal mean-free path curve valid for metals;[43] it is 4~5 Å at about 30 eV, stays around this value up to ~300 eV, and then starts rising linearly with k. All these components should be considered for a reliable assessment of the rate of convergence of the MS series.

JA940067K

(67) Rehr, J. J.; Albers, R. C. *Phys. Rev. B* **1990**, *41*, 8139.